

RESEARCH OUTPUTS / RÉSULTATS DE RECHERCHE

Experimental and theoretical study of a magnetron DC-PECVD acetylene discharge

Fauroux, A.; Vandenabeele, C.; Pflug, A.; Lucas, S.

Published in:

Surface and Coatings Technology

DOI:

[10.1016/j.surfcoat.2020.126195](https://doi.org/10.1016/j.surfcoat.2020.126195)

Publication date:

2020

Document Version

Peer reviewed version

[Link to publication](#)

Citation for published version (HARVARD):

Fauroux, A, Vandenabeele, C, Pflug, A & Lucas, S 2020, 'Experimental and theoretical study of a magnetron DC-PECVD acetylene discharge: Determination of the main species and reactions taking place in the plasma', *Surface and Coatings Technology*, vol. 400, 126195. <https://doi.org/10.1016/j.surfcoat.2020.126195>

General rights

Copyright and moral rights for the publications made accessible in the public portal are retained by the authors and/or other copyright owners and it is a condition of accessing publications that users recognise and abide by the legal requirements associated with these rights.

- Users may download and print one copy of any publication from the public portal for the purpose of private study or research.
- You may not further distribute the material or use it for any profit-making activity or commercial gain
- You may freely distribute the URL identifying the publication in the public portal ?

Take down policy

If you believe that this document breaches copyright please contact us providing details, and we will remove access to the work immediately and investigate your claim.

Manuscript cover page

Surface and Coatings Technology

Keywords:

PIC-MC; Magnetron; C₂H₂; PECVD; Simulation; Mass Spectrometry; DLC

Highlights

- 3D PIC-MC model was set up with a carefully chosen, self-contained plasma chemistry scheme involving 18 species and 150 reactions.
- The spatial distributions of all species differ significantly.
- Density of hydrocarbon ions reaching the substrate grows linearly with power in both simulations and experiments, with matching slopes and relative concentrations.
- Even though electron dissociative collisions are less probable than simple ionizations, the radical species they produce accumulate due to their slower diffusion.
- The model predictions can be extrapolated to the high power-densities used in lab or in production.

Experimental and theoretical study of a magnetron DC-PECVD acetylene discharge: determination of the main species and reactions taking place in the plasma.

A. Fauroux¹, C. Vandenabeele¹, A. Pflug², S. Lucas¹,

¹ Laboratoire d'Analyse par Réactions Nucléaires (LARN), Namur Institute of Structured Matter (NISM), University of Namur, 61 Rue de Bruxelles, 5000 Namur, Belgium

E-mail: antoine.fauroux@unamur.be, Tel: +3281724701, ORCID: 0000-0002-9635-1758

E-mail: cedric.vandenabeele@unamur.be, Tel: +3281725479, ORCID: 0000-0001-7164-3503

E-mail: stephane.lucas@unamur.be, Tel: +32498975282, ORCID: 0000-0003-3229-9855

² Fraunhofer Institute for Surface Engineering and Thin Films IST, Bienroder Weg 54e, 38108 Braunschweig

E-mail: andreas.pflug@ist.fraunhofer.de, Tel: +495312155629

Corresponding author: stephane.lucas@unamur.be, Tel: +32498975282,

Abstract

A mixed PVD/PECVD deposition process of DLC films with acetylene precursor and graphite magnetron target was simulated using a 3D Particle-in-Cell Monte-Carlo (PIC-MC) code. The simulation comprises of a carefully chosen, self-contained plasma chemistry scheme involving 18 species and 150 reactions, and a dynamic deposition model that includes ion subplantation and the creation of dangling bonds. Mass spectroscopic measurements of neutrals and ions have been performed at substrate position in order to validate the simulation's predictions. Despite the difficulty in performing reliable mass spectrometry in reactive plasmas and the impossibility of running PIC-MC simulations with powers and time scales comparable to the experiment, we were able to correlate the simulated and

experimental densities with varying discharge powers and acetylene contents. We showed that the relative concentrations vary spatially within the chamber due to differences in species' diffusion, energy or creation area (plasma or chamber). The power dependence of the hydrocarbon ion densities was linear with similar slopes and relative concentrations in experiments and simulations. This is an indication that our model could be extrapolated to relevant experimental conditions and give quantitative predictions on densities, fluxes and energies of principal species, which could be used as input for film growth simulations. It can also form the basis for simulation frameworks of deposition processes that involve the decomposition of C_2H_2 in low-pressure plasmas (below 1 Pa) with complex reactor geometries and electromagnetic fields.

1. Introduction

Numerical simulation helps to understand the underlying physical mechanisms involved in complex processes and may reduce the need for costly experimental approach of trial and error. This is why the digitalization in the industry calls for representation of each involved production process by its digital twin. Consequently, the development of numerical simulation tools for plasma deposition processes is an ongoing effort of many research groups. For cold plasma systems, the Particle-in-Cell Monte-Carlo (PIC-MC) method has been used to simulate various discharge types [1–7] with the general goal to first compute the density of neutrals and charged particles in the gas phase and second understand or predict the growth of specific coatings.

Among the large variety of coatings, hydrogenated amorphous carbon (a-C:H), a soft form of diamond-like carbon (DLC), are popular amongst scientists and industrials for their advantageous properties, such as moderate hardness, low friction coefficient, chemical inertness and optical transparency, making them practical for biomedical, tribological and

protective applications [8–10]. Nowadays, the development of new deposition methods (like Filtered arc or Catalytic plasma deposition) or new techniques (e.g., High-power impulse magnetron sputtering or HiPIMS) facilitates the production of harder forms of carbon coatings, like tetrahedral amorphous carbon (ta-C), which show improved physical properties compared to softer carbon films [11]. However, the low-pressure plasma deposition in a magnetron reactor with a reactive hydrocarbon precursor such as acetylene remains a popular and flexible method to generate smooth and soft DLC films which relies on combining plasma-enhanced chemical vapor deposition (PECVD) and physical vapor deposition (PVD) [12–14]. It has the advantage to be suitable for industrial upscaling [14] and it is often used in combination with other processes to create more complex film structures like multilayers [8] or doped films [9]. Moreover, this process allows the deposition on more complex substrate shapes, by using various techniques like substrate motion, multiple sources, or bias application to produce more homogenous film [26]. These methods can produce a variety of carbon coatings since the film physical properties can be tuned by adjusting the operational parameters. For example, depending on the pressure films ranging from very smooth to micro-structured can be created [13]. An important challenge is to deposit, in a reproducible way, the same homogeneous coatings on different complex substrate geometries. Commonly faced problems include bad film adhesion to substrates that requires the deposition of interfacial layers [15], or high compressive stress and delamination, which can be reduced by adjusting the bias, temperature or film thickness [16–18]. Inhomogeneity on substrates with complex shapes is another common pitfall, and could be reduced via substrate holder motions or the application of variable bias [19]. The flux ratio between the background gas (usually argon) and the hydrocarbon precursor (most often C_2H_2 or CH_4) can also have a big impact on the H and sp^3 content of films, which are among the most significant parameters for coating properties [8,14,20]. As seen from these few examples, deposition processes are highly

tunable and can become increasingly complex due to the high number of factors impacting the deposited film properties. Moreover, experimental diagnostics give only partial information on particle dynamics and do not allow a clear understanding of these processes.

Unfortunately, not many modelling studies exist on this particular a-C:H deposition method from magnetron sputter sources.

There is an abundant literature on similar processes involving pure PECVD with acetylene in different types of reactors and for different applications but they often involve higher pressures. Mao et al. [21] presented a 1D fluid model of an RF discharge in acetylene, including more than 400 reactions and 78 species (containing up to 12 carbon atoms), based on a previous model developed by De Bleeker et al. [22]. Like in most plasma fluid models, they used a two-term Boltzmann equation solver to obtain the electron energy distribution function (EEDF) and Chapman-Enskog theory for neutral transport. Their findings were successfully compared with the mass spectrometry measurements of Deschenaux et al. [23]. They confirmed, as in other studies [13,22], the prominence of $C_{2n}H_x$ species plasmas due to the strength of acetylene triple bonds, and pointed out the role of anions in nanoparticle formation. Ariskin et al. [24] presented a hybrid model, which consists of a 1D fluid model with 146 chemical reactions and many species including 16 cations and 6 anions, of a capacitively coupled radio frequency discharge (CCRF). But instead of a two-term Boltzmann solver, they used a Particle-in-cell Monte-Carlo (PIC-MC) solver to obtain the electron energy distribution function (EEDF). They compared their results with a simpler approach that uses an approximated Maxwellian EEDF, and found a slight difference in densities and energies of charged species. They also showed that a relatively small amount of acetylene can have an important effect on the plasma behavior: the addition of only 5.8 % of acetylene to the background gas, composed mainly of argon, lowers the plasma density by a factor of 5, and

makes the mixture more electronegative. In another work, Mao et al. [25] used a hybrid model to simulate an inductively coupled plasma reactor for carbon nanotube or nanofiber synthesis from various feed gases, and found that with acetylene, higher decomposition rates and the formation of long neutral and ionic hydrocarbon chains occurred. In the work of Miyagawa et al. [26], a PIC-MC simulation of plasma immersion ion implantation (PIII) in nitrogen and acetylene was presented. In order to study the deposition precursors and their energies, 10 hydrocarbon species were considered ($C_2H_2^+$, $C_2H_2^{2+}$, C_2H^+ , CH^+ , H^+ , C_2H_2 , C_2H , CH_2 , CH , H). Apart from elastic collisions, the authors considered only direct ionization, dissociative ionization and double-ionization of acetylene and nitrogen. They found that a positive pulse followed by a negative one was the most efficient bias mode for making plasma conformal to their substrate. $C_2H_2^+$ and H were the prominent species, but, as they pointed out, this model might not be sufficient to identify deposition precursors, since no chemical reactions nor sticking coefficients were included. Gordillo-Vázquez et al. [27] developed a space-time averaged kinetic model to study the influence of the pressure and power on the deposition of DLC in an RF reactor within a mixture of Ar/ H_2 and 1 % of C_2H_2 . They found that for high content of argon (95 %), the concentration in C_2H , C_2 and C_2^* grows as the pressure decreases. They also found that the electron density is not significantly influenced by the power, but increases with pressure.

Experimental characterization of the plasma chemistry of low-pressure acetylene plasmas is a complex task, due to the great number of possible compounds and high deposition rates. No in-situ experimental studies of the magnetron PECVD in Ar/ C_2H_2 itself exist (to authors' best knowledge). However, there are some studies of this process from the perspective of sample characterization [13,14], and some were conducted on other acetylene-containing plasma discharges. For example, Baby et al. [28] did an experimental study on the chemistry of

Ar/C₂H₂ mixtures in capacitively and inductively coupled RF plasma (CCP and ICP) using mass spectrometric measurements. It was found that the injection of acetylene had an important impact on the discharge voltage, electron temperature and electron density. The dominant ion species for CCP was C₂H₂⁺ followed by Ar⁺ and C₄H₃⁺, whereas for ICP the argon ions dominated. This observation stems from the higher density and greater portion of medium energy (3-11 eV) electrons in ICP plasma discharges, which are below the acetylene ionization threshold at 11.4 eV, but can still ionize argon through the Penning ionization process. The main neutral species were H₂, CH, C₂, C₂H, C₂H₂, C₂H₃, C₂H₄, C₄, C₄H, C₄H₂ and C₄H₃. Similarly to Deschenaux et al. [23], Baby et al. did not observe the heavier species seen by De Bleecker et al. [22] and explained that charge transfer with the dominant argon species might lower the probability of chain polymerizations, hence diminishing the number of heavier hydrocarbons. Thiry et al. [14] noticed a substantial pressure-drop in an acetylene containing magnetron discharge, as did Baby et al. [28]. They attributed it to the dissociation of C₂H₂ and the deposition of generated radicals, as this pressure drop was proportional to the acetylene ratio. The ethynyl radical C₂H has been commonly identified as being the most important DLC growth precursor [13,29,30] due to its abundance and high surface loss probability [31]. This radical is also highly reactive with the background C₂H₂. Benedikt [30] showed that in an expanding thermal plasma (ETP), the C₂H density has a second order behavior with respect to the acetylene flow, since as when the C₂H₂ flow becomes important, C₂H have a higher probability of reacting before reaching the substrate, and diacetylene species (e.g., C₄H₂, C₄H and C₄) become dominant. The author also proposed a quasi-1D chemistry model to demonstrate the role of other radicals in the deposition of a-C:H, like C₃ and C₃H, which are said to originate from C₂H₂ collisions with C and CH radicals and have high sticking coefficients.

As demonstrated above, plasma processes with C_2H_2 involve a high number of species and reaction pathways. The aforementioned numerical studies are mainly based on computational fluid dynamics (CFD) and implement rather complex chemical reaction schemes; still, this allows to address only small or lower-dimensional simulation volumes. In case of magnetron sputtering at pressures below 1 Pa, CFD approaches are no longer valid [32]. Additionally, magnetron discharges are characteristically non-equilibrium processes; the magnetic plasma confinement and the non-thermal emission characteristics of sputtered species play a significant role in the deposition process, which cannot be studied simply with a fluid or hybrid model [32]. Nevertheless, studying a low-pressure process has certain advantages; it greatly simplifies the plasma chemistry and facilitates kinetic simulation approaches like PIC-MC, which are generally more resource-demanding than CFD methods.

The goal of the present study is therefore to simulate a low-pressure magnetron plasma discharge in C_2H_2 in order to predict the main neutral, radical and charged species concentrations. For this purpose, a 3D PIC-MC simulation model including a detailed plasma and surface description was set up. The simulations were validated with mass spectrometric measurements made in an experimental reactor in a similar configuration. This is a stepping stone in a longer effort of the authors to create a complete model of the smooth a-C:H deposition process.

The first part of this article describes the experimental setup and the PIC-MC model. The experimental apparatus is described in section 2.1. The numerical parametrization is described in section 2.2. The plasma chemistry reactions are listed, and their relative importance discussed in section 2.3. Subsequently, the surface reactions for the substrate, chamber walls, and target are presented in section 2.4. Both experimental and numerical results are shown and discussed in section 3. Finally, main conclusions are summarized in section 4.

2. Method Description

2.1 Experimental Setup

For this work, a small-size research reactor already described in [7] was used. The plasma was generated from a DC-powered unbalanced circular magnetron operated in fixed-current mode on a 2 inches graphite target. The pressure was set to 5 mTorr (0.66 Pa) with injection of argon and acetylene behind the cathode. The total mass flow was kept constant during experiments with variable acetylene/argon ratio, keeping a constant total pressure by adjusting the effective pumping speed via a throttle valve. The maximum effective pumping speed with a fully open throttle valve was 70 l s^{-1} as in [7] and the total mass flow was 12, 16 or 20 sccm depending on the experiment. Mass spectrometry measurements of the gas phase were performed using a quadrupole PSM003 mass spectrometer supplied by Hidden Analytical, equipped with a turbo-molecular pump reaching a typical pressure of 10^{-8} mbar and connected to the deposition chamber by a $100 \mu\text{m}$ in diameter extraction orifice, facing the magnetron target at distance of 10 cm. Mass spectrometry measurements of neutrals were performed in residual gas analysis (RGA) mode and in Secondary-ion mass spectrometry (SIMS) mode for the ions. Neutral species entering the mass spectrometer were ionized inside the spectrometer with a 70 eV electron source to allow their detection. In SIMS mode, the detector was calibrated with a low-power pure argon plasma. In order to compare with PIC-MC simulation which are limited in attainable power, measurements were performed with the plasma ignited at power ranging from as low as 5 W up to 200 W (or, in terms of power density, from 0.25 to 9.87 W cm^{-2}), with the aim of estimating the measurements dependence on power.

2.2 Simulation Parameters

A parallelized PIC-MC software running on a Tier-1 cluster and developed at Fraunhofer IST [37, 38] was used. In order to keep the computational time reasonable, the chamber geometry was simplified by considering only a magnetron surrounded by a small bounding box, with a grounded substrate located at 80 mm from the target (see Figure 6). To take advantage of the parallelization, the chamber was cut into several volume segments or “quads”, which are simulated on separate CPUs. To avoid limitations due to too many communications between computing nodes, simulations were kept on single nodes by dividing the simulation volume by 5 in the longitudinal direction and by 2 in both other directions, for a total of 20 quads, or 21 CPUs on the 24 available per nodes. The magnetron, composed of several cylindrical magnets, a metallic yoke, and a graphite target surrounded by a grounded shield, was modelled based on the one used in the experiments. The magnetic field was computed with a boundary element method solver (BEM) from the shape, remanence (1.4 T) and relative permeability (1.05) of the magnets. For a reference, the magnetic field value on the cathode-target surface at the point where the field is tangential to the surface was 0.10 T. The time step in a PIC-MC simulation should be sufficiently small to resolve all relevant physical mechanisms; in particular it should be smaller than the angular frequency of the electron oscillations around the ions. The time step was set to 5×10^{-11} s, as it corresponds to a tenth of the oscillation period for an electron density of $1 \times 10^{15} \text{ m}^{-3}$. Another numerical constraint concerns the cell size, which must remain below 3.4 times the Debye length to properly resolve electrical potential gradients [5,34] which is close to 1 mm in this case. The cell sizes were adapted throughout the chamber (from 0.5 mm to 1.8 mm wide) to keep a more precise sampling close to the target where the particles have high energies. Charged and neutral species are represented with super-particles, which usually comprise a larger number of real particles via a statistical weight factor. Well-chosen weight factors are crucial since a certain amount in the order of 10 particles per cell are needed to give statistically accurate results and

allow all collision pathways to happen, while too many particles render the simulation time and the memory consumption impractical. To ignite the plasma, an initial population of charged species (e, Ar⁺, and C₂H₂⁺) with a small ($1 \times 10^{13} \text{ m}^{-3}$) and uniform density was added. A list of the relevant simulation parameters and statistical weight factors is given in Table I.

2.3 Plasma Chemistry

In all low-pressure plasma sources electrons carry most of the kinetic energy due to their higher mobility, so the most important reactions to consider are the ones between electrons and the background gases. Since acetylene is used in many applications (fusion, thin film deposition, combustion, astrophysics, bio-medicine), an extensive number of measured and calculated cross sections are available. According to our best knowledge, the latest and most complete review of cross-sections of electron-acetylene collisions is given by Song et al. [35]. Collisions for many other hydrocarbons are also available in the article of Janev and Reiter [36], but they lack precision at low energies as they are based on experiments and theoretical calculations for fusion research. For elastic collisions between molecules, the variable soft sphere model was used with parameters taken from [37], and for elastic collisions between electrons and acetylene, which exhibit a resonance around 2.5eV, the recommended cross sections from [35] were used.

Electron impact ionizations (EII) and Dissociative Ionizations (DI) collisions are the main source of ions for molecular precursors like acetylene, as the electrons carry most of the energy and the pressure is too low for the stepwise ionization to occur. The DI reactions are approximately 10 times less probable than the EII, but they are important to include because they are the main producer of new reactive species. Acetylene does not naturally react with the substrates at low temperature. Hence, to deposit thin a-C:H films, it first needs to be

dissociated in more reactive hydrocarbon species. Dissociative excitation (DE) and dissociative recombination (DR) are two other sources for reactive species. DE is similar to DI in terms of cross sections and products for acetylene, but it does not produce charged species. DR is an electron-ion recombination followed by a dissociation (e.g. $C_2H_2^+ + e \rightarrow C_2H + H$), which is a fast reaction with no energy threshold, due to the Coulomb attraction between reactants and the possibility for the excess energy to be distributed amongst the products. Mul and McGowan [38] have provided cross sections for the dissociative recombination of electrons with C_2^+ , C_2H^+ , $C_2H_2^+$ and $C_2H_3^+$. The cross sections for DR reactions with hydrocarbons are weakly dependent on the species, inversely proportional to the electron energy, and really high for low energies ($10^{-13} - 10^{-14} \text{ cm}^2$). DR has higher probability to occur if ions are present in sufficient amounts and electrons have low energies. As we will show later, these are conditions that occur in magnetron discharges away from the plasma bulk. Since the computational limitations of the PIC-MC simulation are related to the absolute collision rate rather than to the number of possible reactions, all the DI, DE and DR reactions for C_2H_2 and C_2H were included.

Electrons can lose energy by inducing excitation of gas species upon impacts in excited states. This energy can be stored as electronic, vibrational, or rotational excitation. The stored electronic excitation energy can sometimes be released by photon emission with a precise wavelength. Several such excitations, followed immediately by photon de-excitation, were included for acetylene with fitted cross sections given in [39]. Vibrationally and rotationally excited states are usually responsible for the major part of energy exchange between electrons and molecules [30] in plasma reactors like ETP. In cold plasmas, if the vibrational-translational relaxation is slow, the vibrational temperature can become much higher than the gas temperature. For example, temperatures of $T_{rot} = 1190 \text{ K}$ and $T_{vib} = 1940 \text{ K}$ were measured

in an ETP plasma with argon and acetylene as precursors, by cavity ring down spectroscopy [40]. Acetylene has five main vibrational excitation energy levels with high cross sections at low energies between 0.1 and 10eV. The effect of vibrationally excited molecules is the increase of gas temperature, and it might have some effect on the electron temperature in the discharge. However, since accounting for the vibrational states in the simulations would turn out to be really costly in terms of memory usage, and since vibrational-translational collisions cross sections are not available in literature but they must however be slow at low pressure, the vibrational excitations were not included in the model. For rotational excitation, the only data available is from the *ab initio* theoretical calculation of Thirumalai et al. [41], which provides the cross sections for several energy level transitions for collisions at 10eV. The reason for this lack of experimental data is the high symmetry of acetylene, which makes those cross sections small and difficult to measure. For these reasons, rotational excitations were also not included in the model.

Argon is notorious for having metastable states [28,42], and can stay excited longer and therefore have higher probability of being able to interact with other particles. Moreover, excited argon can ionize other molecules through the Penning process [43]. For this reason, metastable argon is an interesting species to study in various simulations or experiments involving a C₂H₂/Ar mixture. As reported by Gordillo-Vázquez et al. [44] the reaction $Ar^*(n = 2, ^3P_{0,2}) + C_2H_2 \rightarrow C_2H_2^+ + Ar + e$ has a high rate of $3.5 \times 10^{-10} \text{ cm}^3 \text{ s}^{-1}$. However, the Penning ionization process involves the collision of three reactants, and an ionization through collisions with metastable argons consists of a chain of collisions. This makes these two processes less probable at low pressure, and thus they were not included.

As discussed earlier, Mao et al. [21] demonstrated the importance of anions for the nanoparticle formation and included them with success in their model. Anions are easily

trapped in RF plasma discharges and react more than positive ions. However, since the magnetron mixed PVD/PECVD is a DC discharge, anions will be accelerated towards the substrate, hence anion trapping should not occur. As acetylene and electrons are the main reactants, the most probable source of anions in our case is dissociative electron attachments (DEA) [35]. These reactions are enhanced and exothermic due to the Coulomb attraction, but their resonant character means that they can be caused only by electrons with the right energies. In this work, those reactions were included without their products in order to verify their relative importance without adding complexity.

The first order reactions between energetic electrons and the background gas create ions and several highly reactive radicals that can latter react in fast and sometimes exothermic reactions. In fact, mass spectrometric measurements reveal important concentrations of C_4H_y species as it will be shown in the experimental section (Figure 1 and Figure 2), the presence of which can only be explained by secondary reactions. The computational cost of incorporating more species to a PIC-MC simulation is high because a sufficient amount of all the species in all the cells is required so that statistically accurate results could be obtained. Fortunately, in the case of acetylene, the subset of species generated from secondary reactions is restrained by the fact that the acetylene triple bond is hard to break. It was therefore possible to include most of the reactions between the species generated in first order reactions in our model, with more than 150 reactions for only 18 species. The complete list of reactions incorporated in the model is displayed in Table II and Table III along with typical reaction rates from one simulation.

2.4 Surface Reactions

The surfaces in the numerical model are the target, substrate and chamber walls, delimiting the simulation boundaries (see Figure 6). This simulation box is a subsection of the whole

experimental chamber. While the poles of the power supply are connected to the target and substrate, the surrounding box is set on floating potential, which has a similar effect as a buildup of a space charge in a larger volume. The box acts as a perfect pump for all generated species and as a pressure-controlled source for the two process gases, effectively maintaining a constant pressure in the volume by reinjecting Ar and C₂H₂ molecules with ratios corresponding to their initial partial pressure ratio. The model of a pressure-controlled source acts as an interface between an infinitely large chamber with homogenous gas composition and the simulation volume, which contains the plasma and many species that diffuse only outward. It was shown by changing the box size that this assumption was justified and the bounding box size was considered to have only a minor impact on species concentrations. For the grounded substrate, we developed a film growth model in order to study the film deposition and its effect on species concentrations in the surface vicinity. This model is based on complex amorphous carbon growth models described in literature [8,45–49], and it includes the growth by subplantation of ions and the growth due to the radicals sticking to the dangling bonds at the amorphous hydrogenated carbon film surface. The sticking probability of hydrocarbon radicals is generally lower than 1 and is dependent on the surface state [45,48,49]. In particular, it depends on the availability of dangling bond sites (not terminated by hydrogen bonds) on the surface of the growing a-C:H film. In this model, we included surface state dependence by declaring two types of surface sites, each with specific reactions: high sticking coefficients for radicals on dangling bond and small ones on H-terminated sites, H removal from ions impact, surface bonded hydrogen desorption from reaction with H or C₂H, as well as the fast H absorption reaction on free sites. Some radicals, like the atomic carbon created by target sputtering, have a high sticking probability even on H-terminated sites due to the availability of more than one valence electron. Another important way of creating dangling bonds is by ion impact, and a yield of one surface hydrogen atom by ion

impact was assumed. The complete set of plasma chemical and surface reactions onto the substrate is given in Table IV.

The target surface had to have a different surface model due to the incoming energetic flux of ions. To simplify the simulation, target poisoning was not considered. Hence, to compare the simulation with experiments, we had to stay in the regime of reduced deposition on target compared to target sputtering, or keep plasma ignited for only short periods of time and perform etching between each measurement. With these precautions, it was assumed that the target remains pure graphite. The sputtering of carbon atoms was defined with a 0.03 yield for all ions impinging the target. This yield value comes from SRIM simulations [50] with argon ions impinging a graphite target at 200 eV with normal incidence. This energy was chosen based on typical discharge voltage at these low power densities. With the price of added complexity, different yields for each ion as well as energy and angular dependence could have been used. However, this is a reasonable approximation since Ar^+ is the dominant ionic species in most cases and the discharge voltage does not vary significantly. The sputtered particles energy follows a Thompson distribution [51] defined by a 7.41 eV binding energy. The SRIM calculations showed that ion backscattering is a rare event, so ions are set to be implanted upon impact. However, in order to avoid creating an artificial pressure gradient, the C_2H_2^+ and Ar^+ were set to recombine on the target surface and be released with thermal energy. Upon impact, ions are known to yield secondary emitted electrons (SEE), which is an important mechanism sustaining plasma in magnetrons. The SEE yield was set to 0.11, and electron energies were chosen randomly from a uniform distribution within an energy interval of 0 to 10 eV. These values are standard for metallic targets, but they are unknown for a graphite target (to the authors' knowledge), and graphite probably has a lower SEE yield. According to Depla et al. [52], the SEE yield is reciprocal to the discharge voltage for a given

current. The main impact of a higher discharge voltage would be to increase the energy of ions impinging the substrate, which would in turn slightly increase the electron and carbon yield. The energy gained by electrons traversing the sheath would also rise, which might affect the position of the sheath, as well as the electronic temperature in the plasma bulk [52].

3. Results

3.1 Experimental results

Mass spectrometry measurements were conducted on an argon-acetylene plasma for several flux ratios and imposed currents. To avoid possible bias due to the target pollution, measurements were limited to low powers and short times. Also, before most experiments, the target was etched with a plasma in pure argon at 0.66 Pa and 50 W for several minutes. Figure 1b shows a typical residual gas analysis (RGA) spectrum obtained with 20 % C₂H₂ at 0.02 A and 0.66 Pa. The acetylene ratio is defined as:

$$r = \frac{F_{C_2H_2}}{F_{Ar} + F_{C_2H_2}}, \quad (1)$$

where F_{Ar} and $F_{C_2H_2}$ are the argon and acetylene injected flows. Several known cracking patterns (CPs) [53] are depicted in Figure 1a to help the injected species and pollutants identification. The peaks associated with water vapor (16, 17, and 18 u), and with carbon monoxide (or nitrogen) and carbon dioxide (28, 44 u) were present even before any gas injection, and remained mostly unchanged for all pressures. Therefore, they probably resulted from the presence of residual gases in the chamber and detector. Many peaks can be attributed to acetone, which is used as an acetylene solvent and was present as impurity in the C₂H₂ bottle. Most peaks were unchanged after the plasma ignition (see Figure 1b). The only changes are the lower intensity of acetylene and acetone related peaks (26 and 58 u), and the higher intensity of hydrogen (1 u), dihydrogen (2 u) and diacetylene peaks (48, 49 and 50 u).

Similar RGA measurements were conducted by increasing the power up to 200 W, and no additional peaks were found up to mass 60 u.

All peaks originating from the cracking of the acetylene and acetone molecules receded with plasma ignition, which indicates that the C_2H_2 and C_3H_6O molecules were consumed inside the plasma phase. It was found that subtracting the CPs relative peak intensities from both plasma-on and plasma-off spectrums as in [54] did not reveal remaining concentrations of those product species with more than $1 \times 10^2 - 1 \times 10^3$ count s^{-1} . Some techniques could have been used for circumventing these limitations, e.g., the use of triple differential pumping or Bayesian analysis (see for example [55]). However due to these low intensities and the fact that some peaks are common between the C_2H_2 and C_3H_6O molecules, it was impossible to extract reliable information on the generation of reactive dissociation products like C_2H .

It is clear that the decrease of the acetylene peaks (-1.4×10^5 count s^{-1}) cannot be counterbalanced by the increase of any other peaks ($< 3.4 \times 10^4$ count s^{-1}), even considering possible calibration error or sensitivity bias. This means that acetylene concentration in the chamber diminished significantly. This decrease has to be attributed to loss by ionization or loss by dissociation. Figure 2 presents the main positive ions peaks (empty marker) for 20 % acetylene and varying power, and shows that the main cations were singly-ionized acetylene, with other prominent ionic species being $C_4H_3^+$, $C_4H_2^+$, Ar^+ and $C_2H_3^+$. Interestingly, the relative peak intensities remained similar for all powers and their absolute values increased linearly with increasing power, this is probably due to the linear increase of the electron density with power as further explained in the simulation section. However, the measurements done at the lowest power (2 W) had a much lower intensity and reduced the linear fits quality. This is probably due to cathode pollution, which creates instability in plasma at such low powers, because the carbonated redeposited layer is dielectric and is not etched fast enough.

The measured ion peak intensities were fitted together with the simulated densities, with the commonly made assumption that a quadrupole mass spectrometer gives intensities that are proportional to densities [55]. A common spectrometric intensity-to-density conversion factor for all species with value $1.28 \times 10^8 \text{ m}^{-3} \text{ s count}^{-1}$ was chosen to get the best overall fits between the simulation and experimental lines for hydrocarbons. A good match was observed between simulated and experimentally observed slopes and relative densities for all hydrocarbon ions. However, the Ar^+ density and its spectrometric intensities differed a lot. The origin of that discrepancy is unclear, but it seems that it could be linked to the slight difference of pressure between the simulation and the experiment (see Figure 5 and related discussion below). If the mass spectrometer response for each species was absolutely calibrated or if individual conversion factor were used, the argon ion intensity might be in fact in accordance with its simulated density. However, in the absence of absolute calibration choosing to have only one conversion factor for all spectral lines reduces the number of fitted parameters from 11 parameters in the first case to 15 in the latter.

The RGA measurements with a varying $\text{Ar}/\text{C}_2\text{H}_2$ ratio and fixed current are summarized in Figure 3 next to corresponding neutral densities from simulations. The main peak intensities were obtained by subtracting the average values of every peak during the plasma-on and plasma-off phases for each $\text{Ar}/\text{C}_2\text{H}_2$ ratio at constant initial pressure and pumping speed. This subtraction reveals only the peaks whose intensity increased, hence it is possible that other neutral species were present in the chamber in abundance but masked by the cracking of acetylene and acetone in the detector as discussed above. The main peaks (threshold of $4000 \text{ count s}^{-1}$) were for H, H_2 , C_4H_2 , C_4H , and C_4H_4 . According to [53], the cracking pattern for H_2 contains a peak at mass 1 u which corresponds to only 2 % of the main peak; it therefore cannot explain the observed amount of atomic hydrogen observed (roughly 50 % of H_2

intensity), so atomic hydrogen must be present in the chamber in the spectrometer vicinity. The main neutral species were in order of importance H₂, H and C₄H₂, whereas in the simulation they were C₂H, H, H₂ and C₄H₂. This discrepancy might stem from the short simulation times as explained further in the discussion. However, all measured peak intensities and simulated densities increased linearly with acetylene content which is a sign that the origin of the observed species must be, as in the simulations, linked to the electron dissociations of acetylene hence proportional to the electron and the acetylene density.

The main positive ion peaks were measured in SIMS mode with a varying Ar/C₂H₂ ratio at 16 mA, and the resulting points are shown in Figure 4. Since the detection of ions with a MS facing an unbalanced magnetron can saturate the detector, the distance between the MS and the magnetron were set to 18 cm instead of the 10 cm used for other experiments. At low acetylene content Ar, Ar²⁺ and ArH⁺ were the dominant ionic species, but after only 12.5 % acetylene, C₂H₂⁺ became the dominant species. We observed a decrease of argon related ions intensities for increasing ratios, and an increase of all hydrocarbon ions intensities. The total ion intensity decreased initially with acetylene injection but then increased after a ratio of 7.5% acetylene, following the general increase of hydrocarbon ions. The main hydrocarbon ions were C₂H_{2,3}⁺, C₄H_{2,3,4}⁺, and C₆H_{4,5}⁺, which all contained pair number of carbon atoms. Interestingly, this increase in intensity depended on ions' number of carbon atoms, with a small increasing rate for C₂H_{2,3}⁺ a bigger one for C₄H_{2,3,4}⁺, and an even steeper increase for C₆H_{4,5}⁺. The initial decrease of total ion density, probably associated with a similar decrease in electronic density, could be attributed to several causes, for example: acetylene low ionization threshold and large cross-section compared to argon, cathode pollution, pressure variations. Indeed, while the initial pressure was kept constant at 5 mTorr before plasma ignition, the pressure systematically dropped when the plasma was ignited and when

acetylene was present. This phenomenon is due to the fact that reactive species condensation on the chamber walls affects the total pressure more than the competing effect of acetylene splitting in the plasma, as shown by D. Thiry et al. [14].

Figure 5 presents the intensity of main ion peaks for different initial pressures with a 4% ratio of acetylene and a current set to 100 mA. It suggests that the pressure had indeed a big impact on the measured ion peaks: for a small pressure variation of around 3mTorr (or 0.133 Pa), a variation of more than one order of magnitude of the intensities is observed. One possible explanation of this phenomenon is that at higher pressure, ions have more probability to recombine with low energy electrons, or to react with acetylene creating new ionic species, thus diminishing the number of $C_2H_2^+$ and Ar^+ ions reaching the detector. The pressure change could also have an impact on the electron mean free path, reducing their energy and hence reducing the electronic temperature and ionization rate. Interestingly, Figure 5 shows that $C_2H_2^+$ is promoted for high pressures and its concentration raises above that of Ar^+ , even though acetylene represents only 4 % of the background gas, which means that either acetylene gets ionized easier than argon or charge transfer reactions tend to promote acetylene ions over argon ones.

3.2 Simulation results

Several simulations were run with power setpoints ranging from 0.1 to 1.0 W (5×10^{-3} to 5×10^{-2} W cm⁻²), and relative concentrations of argon and acetylene ranging from 0 % to 90 %, defined as:

$$r = \frac{P_{C_2H_2}}{P_{Ar} + P_{C_2H_2}}, \quad (2)$$

with P_{Ar} and $P_{C_2H_2}$ being the initial partial pressures of argon and acetylene, respectively. A stable plasma ignition was obtained in all cases, with charge densities ranging from 1×10^{14}

to $1 \times 10^{16} \text{ m}^{-3}$, and with a maximum ionization degree of 1×10^{-4} . Typical computation time were as long as 50 h for a physical discharge simulation time of 50 μS . Drifting ionization zones or “spokes” were present on most of the simulations, and can be seen as an asymmetry in Figure 6. For a typical simulation with a power of 0.8 W and an acetylene ratio of 20% the spoke was rotating in the opposite of the $\vec{E} \times \vec{B}$ drift direction with a period of around 30 μs . This phenomenon has been described in recent experimental articles [56] and reproduced with PIC-MC simulations [33]. However, since they were not the primary interest of this study, their effects on densities and other observables were minimized by averaging densities over time and space. The electron energy distribution functions (EEDF) were calculated across the chamber from electrons’ velocity distribution and the results were fitted with Maxwellian or Bi-Maxwellian distribution functions. For the plasma bulk, the EEDFs were Bi-Maxwellian with $T_{e1} \approx 2 \text{ eV}$ and $T_{e2} \approx 10 \text{ eV}$. This Bi-Maxwellian distribution is a known characteristic distribution for electrons in magnetron plasmas. One population of electrons is made highly energetic by the sheath-target potential difference, and another population resulting from ionization in the plasma bulk has a lower mean energy [32, 57]. This feature together with the spokes are often missing from other models (e.g. fluid models) and justify the choice of the PIC-MC approach, as explained in section 1.

The simulation with 20 % acetylene and 0.8 W has been chosen as an arbitrary representative simulation it will be referred as “S₁” in the following to ease discussion. Densities in this simulation were averaged inside cylindrical, 1mm-thick slices across all the chamber. The resulting density profiles for each time step of S₁ from 0 to 50 μs are visible in Figure 7. The equilibrium for charged species was reached faster than for neutrals, as the bulk density of electrons and main ions increased very slowly after 5 μs , whereas C₂H, H, C and CH kept increasing even after 20 μs . For most species, the maximum density was located in the plasma

bulk, at the edge of the plasma sheath, around 5 mm away from the cathode. The main species in the bulk were the radicals C_2H and H , which accumulated gradually slower as their concentrations were approaching an equilibrium. The $C_2H_3^+$, $C_4H_2^+$ and $C_4H_3^+$ density profiles had a maximum outside of the plasma bulk because they were mainly produced by recombination of $C_2H_2^+$ ions with C_2H_2 . The C_2H and H_2 species were distributed more homogeneously than the other radicals because they were produced not only in the bulk but also during recombinations in the rest of the chamber. The density profile of C was nearly a straight line for all time steps, with a slope decreasing with the distance from target. This linear profile results from the fact that sputtered carbon atoms have a high kinetic energy, which induces a fast diffusion and a reduced loss of momentum via collisions with the background gas molecules. In addition to differences in longitudinal profiles, species had different lateral profiles: charged species formed a narrow beam throughout the chamber, due to the unbalanced magnetic field configuration, whereas the radicals formed a wider beam because they diffused thermally from the bulk where they were created. The widest diffusion cone was the one of carbon atoms due to simulation's wide angular distribution for sputtered particles. Figure 8 compares vertical cuts of the densities of C atoms and $C_2H_2^+$ cations and the profile of their respective absorptions onto surfaces. The aforementioned difference in diffusion spread of sputtered atoms and ions can be seen on this figure, as well as the impact it would have in terms of homogeneity of the resulting substrate absorption.

Table II and III contain all the reactions that were included in our model, as well as the observed reaction rates in S_1 , averaged between 30 and 40 μs in the whole simulation volume. From these rates, some conclusions regarding the choice of reactions and species can be made. For example, the main reactions producing new species were indeed the DE and DI reactions, followed by DR ones, as discussed in section 2.3. The DEA were non-neglectable

with rates up to $1 \times 10^{15} \text{ m}^{-3} \text{ s}^{-1}$ for the $e + \text{C}_2\text{H}_2 \rightarrow \text{C}_2\text{H}^- + \text{H}$ reaction. Adding them could indeed be interesting if, for example, more data on anions could be experimentally obtained, or if anions effects on deposition were to be considered. The fastest reactions not involving electrons were charge transfers and reactions between acetylene and C_2H , H or C_2H_2^+ . In particular, the dissociative recombination of C_2H_2 and C_2H_2^+ was responsible for the production of the majority of the diacetylene species.

Figure 9 shows a general view, built upon Figure 7, of the species present in the chamber at a moderate acetylene ratio (i.e., 20%) 40 μs after plasma ignition. The sputtered carbon flux was not among the dominant species as it was always two orders of magnitude less concentrated than the other species. Moreover, this difference increases with the distance. This means that the sputtered atoms contribution to deposition decreases relatively to the hydrocarbon ions and radicals' contributions if the substrate is set further away from the cathode. The sputtered carbon atoms did not participate much in the plasma chemistry since the fastest reaction involving C was $\text{C}_2\text{H}_2^+ + \text{C} \rightarrow \text{C}_3\text{H}^+ + \text{H}$ with a rate of $1 \times 10^{12} \text{ m}^{-3}$ (see Table III). Since the production of sputtered atoms is proportional to the ions flux towards the cathode which is itself proportional to the electronic density and hence to the power, it would be rather simple to extrapolate the C flux towards the substrate for higher powers. The density profile of radicals was decreasing faster with distance than the one of ions, hence the contribution of radicals to film growth compared to the one of sputtered hydrocarbon ions should also depend on the distance from the target and get less important the further the substrate is set. This is an important result to improve film deposition as it shows that the growth precursor concentrations are non-homogenous in the chamber, and therefore the types of films produced via this deposition method will depend on the location of the substrate.

Figure 10 shows the densities in the plasma bulk (defined as a cylindrical volume parallel to the target with a 20 mm radius and 20 mm height) for all species included in the simulation after 20 μs , for many simulations differing from S_1 only in power (right) or only in ratio (left). The averaged densities of all produced species inside the bulk evolved linearly with power and remained proportional to the electron density. In terms of ratio, two populations with constant relative concentrations could be distinguished in Figure 10: the first order species (C_2H_2^+ , C_2H^+ , H , C_2 , H_2 , and CH), which originated mostly in direct reactions between electrons and acetylene, and the second order species (C_4H_3^+ , C_4H_2^+ , C_2H_3^+ , C_2H_3 , and C_4H_2), which were primarily generated in collisions between these first order species and the background acetylene (see Table III). The second population was more sensitive to a change in C_2H_2 , and this stems from the fact that the reaction rates depend on the density of both reactants. Hence, while the first order species varied linearly with the C_2H_2 ratio and the power (Figure 2 and Figure 10), the second order species varied linearly with power but in a quadratic manner with the acetylene ratio. The mean electron density in the bulk increased also linearly with the ratio of acetylene as can be seen in Figure 10 and in the following linear regression fits:

$$\begin{aligned} n_e(\text{ratio}) &= 2.84193 \times 10^{13} \times \text{ratio} + 4.83609 \times 10^{14} [\text{m}^{-3}] (r^2 = 0.8765) \\ n_e(\text{power}) &= 1.54640 \times 10^{15} \times \text{power} + 1.47808 \times 10^{14} [\text{m}^{-3}] (r^2 = 0.9908), \end{aligned} \quad (3)$$

with n_e the electron density. This could be explained by noticing that the lower ionization threshold of acetylene and larger ionization cross-section makes plasma ignition easier in an acetylene rich mixture, and more electrons are generated via ionization for the same power.

3.3 Discussion

In order to compare simulated densities with the mass spectrometric results, the densities were averaged in a cylindrical volume (10 mm height and 20 mm radius) located in front of the

substrate in several simulations with parameters similar to S_1 , but with different powers or ratios. The results compared with mass spectrometric measurements are shown in Figure 2, Figure 3 and Figure 4. Despite the low power and the short simulation time, the simulated ion densities and the experimental ones were tightly correlated, as can be seen in Figure 2. Indeed, the main hydrocarbon ions in the simulations were $C_2H_2^+$, $C_4H_3^+$, $C_4H_2^+$, and $C_2H_3^+$, respectively, and their densities varied linearly with power with similar relative concentrations. However, the Ar^+ densities were higher than the $C_2H_2^+$ one in the simulation, while the spectrometric measurements suggest that it should be the opposite.

Some reactions were more important away from the plasma bulk rather than close to it. For example, the dissociative recombinations have a high probability of occurring at lower energies, meaning they play a significant role far from the target, where the electron temperature remained around 2 eV. Similarly, reactions between ions, molecules and radicals occurred principally away from the plasma where they were generated, and hence the concentrations of the different species evolved differently across the chamber, as seen in Figure 7. For example, due to the acetylene molecule polarizability, the charge transfer with the argon ion is a fast and even exothermic reaction [60] that will tend to promote the acetylene ions over the argon ones:



Indeed, this reaction happened at a very fast rate in the simulations (around $8.3e^{17} \text{ m}^{-3} \text{ s}^{-1}$) as seen in Table III.

The mass spectrometric measurements showed that the ions peaks intensities decrease with pressure, that the $C_2H_2^+$ ions get promoted at higher pressure over the Ar^+ ones and that an increased C_2H_2 ratio lead to a decreased ion count. All these observations suggest that

collisions like charge transfers and ions recombinations which happen on the ions' path towards the substrate (or detector) and that are amplified at higher pressure or higher C_2H_2 ratio are important and could explain for example the discrepancy observed between the simulated and measured Ar^+ density in Figure 2. Indeed, if the simulation were run for longer times, or if the pressure in the simulation was higher, the charge transfer between Ar^+ and $C_2H_2^+$ would have favored $C_2H_2^+$ density over Ar^+ ones even more. Nonetheless, the good agreement of the slopes and relative densities of hydrocarbon ions between simulations and experiments in Figure 2, is a validation of the simulated ions production in the plasma and of the latter reactions in the chamber as the observed hydrocarbon ion species depend on both mechanisms.

The evolution of ions densities with acetylene ratio, presented in Figure 4 and Figure 10, showed a good qualitative agreement between simulation and experiments. There were some discrepancies between the two figures, for example the point where the density of $C_2H_2^+$ crosses the one of Ar^+ is around 12.5 % in the experiment, while it is closer to 50 % in the simulations. However, we observed in both cases an increase of hydrocarbon ion densities proportional to the acetylene ratio. In particular, species identified in Figure 10 as “First-order” and “Second order” are clearly identifiable on Figure 4. A notable exception to this comparison is the $C_2H_3^+$ ions. They seem to follow the evolution of $C_2H_2^+$ and C_2H^+ on Figure 4, placing them in the “First-order” group, even though they clearly belong to the “Second-order” group based on their evolution in the simulations, as seen on Figure 10. This probably stems from the fact that $C_2H_3^+$ is produced mainly via the addition of H to $C_2H_2^+$ and, as explained earlier, radical densities did not reach equilibrium during simulations.

Figure 3 shows the dependence of neutrals densities on the ratio in the simulations and experiments. It shows that the evolutions were still linear in both cases, but the main species

in the simulations were C_2H and H whereas, experimentally, C_2H could not be observed, and the H intensity was smaller than that of H_2 . However, as Figure 7 reveals, the non-charged species did not attain an equilibrium and the concentrations of C_2H and H diminished in favor of C_4H_2 species and H_2 , as most molecule-molecule reactions incorporated in the model tends to favor C_4H_2 and H_2 species over C_2H and H (see Table III). As can be seen in Figure 7, the accumulation of radicals was too slow to stabilize in several microseconds, even in this small chamber, and will require longer simulation times in the range of milliseconds to achieve stability. Some simulations were run for up to several hundred microseconds, but we found that the surface model has a decisive influence on the densities at equilibrium. Since the prime interest of this study was the plasma chemistry and not the deposition model, the simulation time were kept at several tenth microseconds which consequently allowed us to study a wider range of parameters in a realistic timeframe. This had an impact on the predictions given on neutrals' density in front the substrate (see Figure 3). However, even the radical seemed to be already at equilibrium in the plasma bulk region (see Figure 7 and Figure 10), which means that the "plasma source" would remain as presented, even for longer simulations.

One of the main limitations of the model presented here, common with most PIC-MC simulations, was the low power at which the simulations were run, with a maximum power of 1.2 W attained in this study, far from current applications with typical powers of several hundreds of watts. However, the main effect of a power raise was an increase of the electron density, followed by a proportional increase of all the plasma products (see Figure 10). This is probably due to the fact that in magnetron reactors, electron density can directly be linked to the discharge power, whereas the electron temperature remains almost constant for a wide range of power [59]. According to [30] reaction rates can be calculated from the following equation:

$$R_{AB} = n_A n_B \iint [\overline{v_{rel}} \sigma_{AB}(v_{rel}) f_A(\overline{v_A}) f_B(\overline{v_B})] d\overline{v_A} d\overline{v_B}, \quad (5)$$

with n_A , $\overline{v_A}$, and f_A the densities, velocities and density function of reactant A , $\overline{v_{rel}}$ the relative velocity, and σ_{AB} the cross section of the reaction. For all collisions between electrons and acetylene the only parameter from Equation 5 that varies with power is the electron density. Hence, the first order reactions' rate, and consequently their products, will remain proportional to the electronic density and increase linearly with power. Therefore, the power scaling of the results should be possible as long as the produced species concentrations remain small with respect to the background gas. This is only true for low ionization degree.

4. Conclusions

The magnetron DC discharge with a graphite target in a mixture of acetylene and argon was simulated with a PIC-MC model and compared with mass spectrometric measurements, in order to gain insight on the otherwise difficult to observe reactive plasma chemistry of magnetron PECVD. The set of species and reactions was carefully chosen to include enough complexity to render most physicochemical mechanisms of actual discharges, but reduced to a minimal set to lower the computational cost. The influence of the acetylene and argon ratio and the power on the discharge was investigated. It was demonstrated that the injection of acetylene changes the electron density and consequently the concentration of plasma-generated products and sputtered particles even at very low concentrations. This model includes the hyperthermal sputtering of carbon from the target and all principal first order reactions. It also includes their products, and a set of fast secondary reactions that these species undergo on their way to the substrate. Simulations were run at low power due to inherent limitations of PIC-MC models, but it was shown that all densities in the plasma bulk evolved linearly with the discharge power. Good correspondence between simulations and

experiments of mass spectrometry was obtained with respect to ions, as the densities of hydrocarbon ions arriving at the substrate grew with the discharge power with the same slopes and relative concentrations in both cases. Good qualitative agreement between simulations and experiments was obtained for density variations with the acetylene ratio. It was possible to identify groups of reactive species from the rate at which their density increased with the acetylene ratio; with primary reactions involving electrons and secondary reactions involving the products of first ones and the background acetylene,

One important results of this study is to show that the spatial distribution of different species can differ a lot: ions are concentrated in a beam due to the unbalanced magnetic field, radicals have surprisingly high concentrations and spread profiles due to their slow diffusion, and sputtered particles form a wide beam, the concentration of which weakens faster with distance than for other species. This implies that the growing film precursor fluxes could be very different depending on the location of the substrate within the chamber. A dynamic surface chemistry model, which relies on defining different sets of reactions on hydrogen-terminated sites and dangling bonds sites, was introduced to get more realistic absorption reactions at the substrate. However, the equilibrium of radical species was not yet attained despite simulating up to several hundred microseconds. The primary focus of this study was to properly define the plasma source and the chemistry inside the chamber. In order to give prediction on deposition speed and film quality, further refinements of the surface model as well as longer simulations would be required.

Despite the difficulty to get reliable mass spectrometric measurements in a PECVD reactor and to run simulations with comparable power and time scales as in experiments, it was possible to correlate simulated and measured species concentrations with varying power and

ratio. To our knowledge, these PIC-MC simulations are the first to include this many species and reactions in a fully 3D and self-consistent kinetic plasma model.

5. Acknowledgments

The authors M. Fauroux and S. Lucas gratefully acknowledge the financial support of the Walloon region under the FEDER and 3DCOATER-5: Convention N° 1610258, project 3215. The present research benefited from computational resources made available on the Tier-1 supercomputer of the “Fédération Wallonie-Bruxelles”, infrastructure funded by “La region Wallone” under the grant agreement n°1117545. It was also part of the “DLC plus” project under the Convention SPW n°1710252, CORNET CALL.

6. References

- [1] T. Melzig, M. Siemers, A. Pflug, R. Rank, 3D PIC-MC simulation of anode effects in dual magnetron discharges, *Surf. Coatings Technol.* 241 (2014) 30–32. <https://doi.org/10.1016/j.surfcoat.2013.10.024>.
- [2] V. Ivanov, O. V. Proshina, T. Rakhimova, A. Rakhimov, D. Herrebout, A. Bogaerts, Comparison of a one-dimensional particle-in-cell-Monte Carlo model and a one-dimensional fluid model for a CH₄/H₂ capacitively coupled radio frequency discharge, *J. Appl. Phys.* 91 (2002) 6296–6302. <https://doi.org/10.1063/1.1461895>.
- [3] O. V. Proshina, T. V. Rakhimova, A.T. Rakhimov, A particle-in-cell Monte Carlo simulation of an rf discharge in methane: Frequency and pressure features of the ion energy distribution function, *Plasma Sources Sci. Technol.* 15 (2006) 402–409. <https://doi.org/10.1088/0963-0252/15/3/015>.
- [4] M. Siemers, A. Pflug, T. Melzig, K. Gehrke, A. Weimar, B. Szyszka, Model based investigation of Ar ion damage in DC magnetron sputtering, *Surf. Coatings Technol.* 241 (2014) 50–53. <https://doi.org/10.1016/j.surfcoat.2013.09.025>.
- [5] D. Tskhakaya, K. Matyash, R. Schneider, F. Taccogna, The Particle-In-Cell method, *Contrib. to Plasma Phys.* (2007). <https://doi.org/10.1002/ctpp.200710072>.
- [6] S. Mathioudaki, C. Vandenabeele, R. Tonneau, A. Pflug, S. Lucas, Characterization of a pulsed low pressure argon discharge in a cylindrical magnetron reactor by plasma diagnostic and 3D plasma modeling, *J. Vac. Sci. Technol. A.* 37 (2019) 031301. <https://doi.org/10.1116/1.5064690>.
- [7] R. Tonneau, P. Moskovkin, A. Pflug, S. Lucas, TiO_x deposited by magnetron sputtering: A joint modelling and experimental study, *J. Phys. D: Appl. Phys.* 51 (2018) 195202. <https://doi.org/10.1088/1361-6463/aabb72>.
- [8] J. Robertson, Diamond-like amorphous carbon, *Mater. Sci. Eng. R Reports.* 37 (2002) 129–281. [https://doi.org/10.1016/S0927-796X\(02\)00005-0](https://doi.org/10.1016/S0927-796X(02)00005-0).
- [9] J. Vetter, 60 years of DLC coatings: Historical highlights and technical review of cathodic arc processes to synthesize various DLC types, and their evolution for industrial applications, *Surf. Coatings Technol.* 257 (2014) 213–240. <https://doi.org/10.1016/j.surfcoat.2014.08.017>.
- [10] J. Robertson, Diamond-Like Carbon Films, Properties and Applications, *Compr. Hard Mater.* 3 (2014) 101–139. <https://doi.org/10.1016/B978-0-08-096527-7.00043-X>.
- [11] S. Neuville, New application perspective for tetrahedral amorphous carbon coatings, *QScience Connect.* (2014). <https://doi.org/10.5339/connect.2014.8>.
- [12] C. Lopez-Santos, J.L. Colaux, J.C.C. Gonzalez, S. Lucas, Investigation of the growth mechanisms of a-CH_x coatings deposited by pulsed reactive magnetron sputtering, *J. Phys. Chem. C.* 116 (2012) 12017–12026. <https://doi.org/10.1021/jp300697s>.
- [13] V. De Vriendt, S.M. Miladinovic, J.L. Colaux, F. Maseri, C.L. Wilkins, S. Lucas, Growth mechanisms involved in the synthesis of smooth and microtextured films by acetylene magnetron discharges, *Langmuir.* 27 (2011) 8913–8922. <https://doi.org/10.1021/la2003035>.

- [14] D. Thiry, A. De Vreese, F. Renaux, J.L. Colaux, S. Lucas, Y. Guinet, L. Paccou, E. Bousser, R. Snyders, Toward a Better Understanding of the Influence of the Hydrocarbon Precursor on the Mechanical Properties of a-C:H Coatings Synthesized by a Hybrid PECVD/PVD Method, *Plasma Process. Polym.* 13 (2016) 316–323. <https://doi.org/10.1002/ppap.201500050>.
- [15] A. Grill, B. Meyerson, V. Patel, Interface modifications for improving the adhesion of a-C:H films to metals, *J. Mater. Res.* 3 (1988) 214–217. <https://doi.org/10.1557/JMR.1988.0214>.
- [16] D. Sheeja, B.K. Tay, K.W. Leong, C.H. Lee, Effect of film thickness on the stress and adhesion of diamond-like carbon coatings, *Diam. Relat. Mater.* 11 (2002) 1643–1647. [https://doi.org/10.1016/s0925-9635\(02\)00109-7](https://doi.org/10.1016/s0925-9635(02)00109-7).
- [17] J. Zelez, Low-stress diamondlike carbon films, *J. Vac. Sci. Technol. A Vacuum, Surfaces, Film.* 1 (1983) 305–307. <https://doi.org/10.1116/1.572119>.
- [18] A. Grill, V. Patel, B.S. Meyerson, Optical and tribological properties of heat-treated diamond-like carbon, *J. Mater. Res.* 5 (1990) 2531–2537. <https://doi.org/10.1557/JMR.1990.2531>.
- [19] Y. Hirata, J. Choi, Deposition of a-C:H films on inner surface of high-aspect-ratio microchannel, *J. Appl. Phys.* 120 (2016) 065305. <https://doi.org/10.1063/1.4960694>.
- [20] Y.Y. Wang, Y. Ye, H. Li, L. Ji, Y.Y. Wang, X. Liu, J. Chen, H. Zhou, Microstructure and tribological properties of the a-C:H films deposited by magnetron sputtering with CH₄/Ar mixture, *Surf. Coatings Technol.* 205 (2011) 4577–4581. <https://doi.org/10.1016/j.surfcoat.2011.03.120>.
- [21] M. Mao, J. Benedikt, A. Consoli, A. Bogaerts, New pathways for nanoparticle formation in acetylene dusty plasmas: a modelling investigation and comparison with experiments, *J. Phys. D. Appl. Phys.* 41 (2008) 225201. <https://doi.org/10.1088/0022-3727/41/22/225201>.
- [22] K. De Blecker, A. Bogaerts, W. Goedheer, Detailed modeling of hydrocarbon nanoparticle nucleation in acetylene discharges, *Phys. Rev. E - Stat. Nonlinear, Soft Matter Phys.* 73 (2006) 1–16. <https://doi.org/10.1103/PhysRevE.73.026405>.
- [23] C. Deschenaux, A. Affolter, D. Magni, C. Hollenstein, P. Fayet, Investigations of CH₄, C₂H₂ and C₂H₄ dusty RF plasmas by means of FTIR absorption spectroscopy and mass spectrometry, *J. Phys. D. Appl. Phys.* 32 (1999) 1876–1886. <https://doi.org/10.1088/0022-3727/32/15/316>.
- [24] D.A. Ariskin, I. V. Schweigert, A.L. Alexandrov, A. Bogaerts, F.M. Peeters, Modeling of chemical processes in the low pressure capacitive radio frequency discharges in a mixture of Ar/C₂H₂, *J. Appl. Phys.* 105 (2009) 1–11. <https://doi.org/10.1063/1.3095760>.
- [25] M. Mao, A. Bogaerts, Investigating the plasma chemistry for the synthesis of carbon nanotubes/nanofibres in an inductively coupled plasma enhanced CVD system: the effect of different gas mixtures, *J. Phys. D. Appl. Phys.* 43 (2010) 205201. <https://doi.org/10.1088/0022-3727/43/20/205201>.
- [26] Y. Miyagawa, H. Nakadate, M. Tanaka, M. Ikeyama, S. Nakao, S. Miyagawa, PIC simulation of N₂ and C₂H₂ plasma behavior around plural objects, *Surf. Coatings*

- Technol. 201 (2007) 8414–8419. <https://doi.org/10.1016/j.surfcoat.2006.03.067>.
- [27] F.J. Gordillo-Vázquez, J.M. Albella, Influence of the pressure and power on the non-equilibrium plasma chemistry of C₂, C₂H, C₂H₂, CH₃ and CH₄ affecting the synthesis of nanodiamond thin films from C₂H₂(1%)/H₂/Ar-rich plasmas, *Plasma Sources Sci. Technol.* 13 (2004) 50. <https://doi.org/10.1088/0963-0252/13/1/007>.
- [28] A. Baby, C.M.O.O. Mahony, P.D. Maguire, Acetylene-argon plasmas measured at a biased substrate electrode for diamond-like carbon deposition: I. Mass spectrometry, *Plasma Sources Sci. Technol.* 20 (2011) 015003. <https://doi.org/10.1088/0963-0252/20/1/015003>.
- [29] J.R. Doyle, Chemical kinetics in low pressure acetylene radio frequency glow discharges, *J. Appl. Phys.* 82 (1997) 4763. <https://doi.org/10.1063/1.366333>.
- [30] J. Benedikt, Acetylene Chemistry in Remote Plasmas: Implications for the a-C:H Growth Mechanism, 2004. <https://doi.org/10.6100/IR581182>.
- [31] C. Hopf, T. Schwarz-Selinger, W. Jacob, A. Von Keudell, Surface loss probabilities of hydrocarbon radicals on amorphous hydrogenated carbon film surfaces, *J. Appl. Phys.* 87 (2000) 2719–2725. <https://doi.org/10.1063/1.372246>.
- [32] A. Bogaerts, E. Bultinck, I. Kolev, L. Schwaederlé, K. Van Aeken, G. Buyle, D. Depla, Computer modelling of magnetron discharges, *J. Phys. D. Appl. Phys.* 42 (2009) 194018. <https://doi.org/10.1088/0022-3727/42/19/194018>.
- [33] A. Pflug, M. Siemers, T. Melzig, L. Schäfer, G. Bräuer, Simulation of linear magnetron discharges in 2D and 3D, *Surf. Coatings Technol.* 260 (2014) 411–416. <https://doi.org/10.1016/j.surfcoat.2014.09.042>.
- [34] A.B. Langdon, Effects of the spatial grid in simulation plasmas, *J. Comput. Phys.* (1970). [https://doi.org/10.1016/0021-9991\(70\)90024-0](https://doi.org/10.1016/0021-9991(70)90024-0).
- [35] M.-Y. Song, J.-S. Yoon, H. Cho, G.P. Karwasz, V. Kokoouline, Y. Nakamura, J. Tennyson, Cross Sections for Electron Collisions with Hydrogen Molecules, *J. Phys. Chem. Ref. Data.* 37 (2008) 913–931. <https://doi.org/10.1063/1.2838023>.
- [36] R.K. Janev, D. Reiter, Collision processes of C₂, 3Hy and C₂, 3Hy⁺ hydrocarbons with electrons and protons, *Phys. Plasmas.* 11 (2004) 780–829. <https://doi.org/10.1063/1.1630794>.
- [37] T.J. Bartel, S. Plimpton, M.A. Gallis, Icarus: A 2D Direct Simulation Monte Carlo (DSMC) Code for Multi-Processor Computers User's Manual-v10.0, (2001).
- [38] P.M. Mul, J.W. McGowan, Dissociative recombination of C₂⁺, C₂H⁺, C₂H₂⁺ and C₂H₃⁺, *Astrophys. J.* 237 (1980) 749. <https://doi.org/10.1086/157921>.
- [39] T. Shirai, T. Tabata, H. Tawara, Y. Itikawa, Analytic cross sections for electron collisions with hydrocarbons: CH₄, C₂H₆, C₂H₄, C₂H₂, C₃H₈, and C₃H₆, *At. Data Nucl. Data Tables.* 80 (2002) 147–153. <https://doi.org/10.1006/adnd.2001.0878>.
- [40] R. Engeln, K.G.Y. Letourneur, M.G.H. Boogaarts, M.C.M. van de Sanden, D.C. Schram, Detection of CH in an expanding argon/acetylene plasma using cavity ring down absorption spectroscopy, *Chem. Phys. Lett.* 310 (1999) 405–410. [https://doi.org/10.1016/S0009-2614\(99\)00810-6](https://doi.org/10.1016/S0009-2614(99)00810-6).
- [41] D. Thirumalai, K. Onda, D. Truhlar, Elastic scattering and rotational excitation of a

- polyatomic molecule by electron impact: Acetylene, *J. Chem. Phys.* 526 (1981).
<https://doi.org/10.1063/1.440804>.
- [42] V. Sushkov, A.-P. Herrendorf, R. Hippler, Metastable argon atom density in complex argon/acetylene plasmas determined by means of optical absorption and emission spectroscopy, *J. Phys. D. Appl. Phys.* 49 (2016) 425201. <https://doi.org/10.1088/0022-3727/49/42/425201>.
- [43] A. Fridman, *Plasma Chemistry*, 2008. <https://doi.org/10.1017/CBO9780511546075>.
- [44] F.J. Gordillo-Vázquez, J.M. Albella, Distinct nonequilibrium plasma chemistry of C₂ affecting the synthesis of nanodiamond thin films from C₂H₂(1%)/H₂/Ar-rich plasmas, *J. Appl. Phys.* 94 (2003) 6085–6090. <https://doi.org/10.1063/1.1617362>.
- [45] J. Benedikt, Plasma-chemical reactions: low pressure acetylene plasmas, *J. Phys. D. Appl. Phys.* 43 (2010) 43001. <https://doi.org/10.1088/0022-3727/43/4/043001>.
- [46] J.E. Butler, R.L. Woodin, L.M. Brown, P. Fallon, Thin Film Diamond Growth Mechanisms, *Philos. Trans. R. Soc. A Math. Phys. Eng. Sci.* 342 (1993) 209–224. <https://doi.org/10.1098/rsta.1993.0015>.
- [47] C. Hopf, A. von Keudell, W. Jacob, Chemical sputtering of hydrocarbon films by low-energy Ar ion and H atom impact, *Nucl. Fusion.* 42 (2002) L27–L30. <https://doi.org/10.1088/0029-5515/42/12/101>.
- [48] A. Von Keudell, M. Meier, C. Hopf, Growth mechanism of amorphous hydrogenated carbon, *Diam. Relat. Mater.* 11 (2002) 969–975. [https://doi.org/10.1016/S0925-9635\(01\)00553-2](https://doi.org/10.1016/S0925-9635(01)00553-2).
- [49] Y. Lifshitz, S.R. Kasi, J.W. Rabalais, W. Eckstein, Subplantation model for film growth from hyperthermal species, *Phys. Rev. B.* 41 (1990) 10468–10480. <https://doi.org/10.1103/physrevb.41.10468>.
- [50] J.F. Ziegler, M.D. Ziegler, J.P. Biersack, SRIM – The stopping and range of ions in matter (2010), *Nucl. Instruments Methods Phys. Res. Sect. B Beam Interact. with Mater. Atoms.* 268 (2010) 1818–1823. <https://doi.org/10.1016/j.nimb.2010.02.091>.
- [51] M.W. Thompson, Physical mechanisms of sputtering, *Phys. Rep.* 69 (1981) 335–371. [https://doi.org/10.1016/0370-1573\(81\)90106-X](https://doi.org/10.1016/0370-1573(81)90106-X).
- [52] D. Depla, G. Buyle, J. Haemers, R. De Gryse, Discharge voltage measurements during magnetron sputtering, *Surf. Coatings Technol.* 200 (2006) 4329–4338. <https://doi.org/10.1016/j.surfcoat.2005.02.166>.
- [53] William E. Wallace, NIST Chemistry webBook, NIST Standard Reference Database Number 69, National Institute of Standards and Technology, Gaithersburg MD, 2020. <https://doi.org/https://doi.org/10.18434/T4D303>.
- [54] M. Buddhadasa, C.R. Vandenabeele, R. Snyders, P.-L. Girard-Lauriault, Single source precursor vs. precursor mixture for N-rich plasma polymer deposition: Plasma diagnostics and thin film analyses, *Plasma Process. Polym.* 14 (2017) 1700030. <https://doi.org/10.1002/ppap.201700030>.
- [55] J. Benedikt, A. Hecimovic, D. Ellerweg, A. Von Keudell, Quadrupole mass spectrometry of reactive plasmas, *J. Phys. D. Appl. Phys.* 45 (2012). <https://doi.org/10.1088/0022-3727/45/40/403001>.

- [56] A. Anders, P. Ni, J. Andersson, Drifting ionization zone in DC magnetron sputtering discharges at very low currents, *IEEE Trans. Plasma Sci.* 42 (2014) 2578–2579. <https://doi.org/10.1109/TPS.2014.2334601>.
- [57] N. Brenning, J.T. Gudmundsson, D. Lundin, T. Minea, M.A. Raadu, U. Helmersson, The role of Ohmic heating in dc magnetron sputtering, *Plasma Sources Sci. Technol.* 25 (2016) 65024. <https://doi.org/10.1088/0963-0252/25/6/065024>.
- [58] A. Bogaerts, E. Bultinck, M. Eckert, V. Georgieva, M. Mao, E. Neyts, L. Schwaederlé, Computer modeling of plasmas and plasma-surface interactions, *Plasma Process. Polym.* 6 (2009) 295–307. <https://doi.org/10.1002/ppap.200800207>.
- [59] S.Z. Wu, Dependence of plasma characteristics on dc magnetron sputter parameters, *J. Appl. Phys.* 98 (2005). <https://doi.org/10.1063/1.2112177>.
- [60] M. Tsuji, H. Kouno, K. Matsumura, T. Funatsu, Y. Nishimura, H. Obase, H. Kugishima, K. Yoshida, Dissociative charge-transfer reactions of Ar⁺ with simple aliphatic hydrocarbons at thermal energy, *J. Chem. Phys.* 98 (1993) 2011–2022. <https://doi.org/10.1063/1.46423>.

7. Tables

Table I Physical and numerical parameters of the simulations

Domain size	$100 \times 72 \times 72$	[mm]
Input power	0.2 – 1.2	[W]
Input power density	$9.8 \times 10^{-5} - 5.9 \times 10^{-5}$	[W.cm ⁻²]
Temperature	300	[K]
Species	<i>Ar, Ar⁺, C₂H₂, C₂H₂⁺, H, C₂H, C₂H⁺, CH, C₂, H₂, C, C₄H₂, C₂H₃, C₄H₂⁺, C₄H₃⁺, C₂H₃⁺</i>	
Pressure	0.6	[Pa]
Magnetron radius	25.4	[mm]
Magnets remanence	1.4	[T]
Cell size	0.5 – 1.8	[mm]
Arrangement of simulation volume segments	5 × 2 × 2	
Time step width	5×10^{-11}	[s]
Maximum physical simulation time, and related computation time	$100 \times 10^{-6}, 4 \times 10^5$	[s]
CPU cores used	21	
Weight factors <i>Ar, C₂H₂</i>	$1 \times 10^{10} \times ratio$	
Weight factors <i>e, Ar⁺, C₂H₂⁺</i>	1.4×10^5	
Weight factors for all other species	$6 \times 10^2 - 1.7 \times 10^4$	
Sampling for the power dissipation	1×10^{-7}	[s]
Carbon Yield	0.03	
Secondary electron emission Yield	0.11	

Table II Collisions involving electrons included in the model and their averaged rates between 30 and 40 μ s in the overall chamber for the S₁ simulation.

Reaction	Name	Rate [m ⁻³ .s ⁻¹]
$e + Ar \rightarrow 2 e + Ar^+$	Ionization	2.09E+19
$e + Ar \rightarrow e + Ar^*$	Total excitation	2.01E+19
$e + C_2H_2 \rightarrow 2 e + C_2H_2^+$	Ionization	9.18E+18
$e + C_2H_2 \rightarrow C_2H + H + e$	Dissociative excitation	3.72E+18
$e + C_2H_2 \rightarrow 2 e + C_2H^+ + H$	Dissociative ionization	1.36E+18
$e + C_2H_2 \rightarrow C_2 + H_2 + e$	Dissociative excitation	9.59E+17
$e + C_2H_2 \rightarrow C + CH_2 + e$	Dissociative excitation	4.49E+17
$e + C_2H_2 \rightarrow C_2 + 2 H + e$	Dissociative excitation	3.17E+17
$e + C_2H_2 \rightarrow 2 CH + e$	Dissociative excitation	3.08E+17
$e + C_4H_2^+ \rightarrow C_4H + H$	Dissociative recombination	3.06E+17
$e + C_2H_2 \rightarrow 2 e + CH^+ + CH$	Dissociative ionization	2.56E+17
$e + C_2H_2 \rightarrow 2 e + C_2^+ + H_2$	Dissociative ionization	2.43E+17
$e + C_2H_2 \rightarrow 2 e + H^+ + C_2H$	Dissociative ionization	2.34E+17
$e + C_4H_3^+ \rightarrow C_4H + H_2$	Dissociative recombination	1.88E+17
$e + C_4H_3^+ \rightarrow C_4H_2 + H$	Dissociative recombination	1.88E+17
$e + C_2H_2 \rightarrow 2 e + C^+ + CH_2$	Dissociative ionization	1.07E+17
$e + C_4H_2^+ \rightarrow 2 C_2H$	Dissociative recombination	1.03E+17
$e + C_2H_2 \rightarrow e + C_2H_2^*$	Electronic excitations (sum)	1.07E+17
$e + C_2H \rightarrow 2 e + C_2H^+$	Ionization	4.44E+15
$e + C_2H \rightarrow C_2 + H + e$	Dissociative excitation	1.42E+15
$e + C_2H_2 \rightarrow C_2H^- + H$	Electron attachment	1.13E+15
$e + C_2H_2^+ \rightarrow C_2H + H$	Dissociative recombination	9.53E+14
$e + C_2H_2 \rightarrow H^- + C_2H$	Electron attachment	6.17E+14
$e + H_2 \rightarrow e + H_2^*$	Excitations (sum)	1.63E+15

$e + C_2H_2^+ \rightarrow C_2 + 2 H$	<i>Dissociative recombination</i>	5.65E+14
$e + C_2H_2^+ \rightarrow 2 CH$	<i>Dissociative recombination</i>	3.2E+14
$e + C_2H \rightarrow C + CH + e$	<i>Dissociative excitation</i>	3.09E+14
$e + C_2H \rightarrow 2 e + C_2 + H$	<i>Dissociative ionization</i>	3.08E+14
$e + H_2 \rightarrow 2 e + H_2^+$	<i>Ionization</i>	1.64E+14
$e + C_2H_2 \rightarrow C_2^- + H_2$	<i>Electron attachment</i>	1.23E+14
$e + C_2H^+ \rightarrow C_2 + H$	<i>Dissociative recombination</i>	9.23E+13
$e + C_2H^+ \rightarrow CH + C$	<i>Dissociative recombination</i>	7.45E+13
$e + C_2H \rightarrow 2 e + C_2 + H +$	<i>Dissociative ionization</i>	7.01E+13
$e + C_2H \rightarrow 2 e + CH^+ + C$	<i>Dissociative ionization</i>	6.66E+13
$e + C_2H \rightarrow 2 e + C^+ + CH$	<i>Dissociative ionization</i>	5.61E+13
$e + C_2H^+ \rightarrow 2 C + H$	<i>Dissociative recombination</i>	3.6E+13
$e + H_2 \rightarrow e + 2 H$	<i>Dissociative excitation</i>	2.84E+13

Table III Collisions that does not involve electrons included in the model and their averaged rates between 30 and 40 μ s in the overall chamber for the simulation S_I.

Reaction	Rate [$m^{-3} \cdot s^{-1}$]
$Ar^+ + Ar \rightarrow slow Ar^+ + Ar$	5,42E+18
$H + C_2H_2 \rightarrow C_2H_3$	1,91E+18
$C_2H_2 + Ar^+ \rightarrow Ar + C_2H_2^+$	8,3E+17
$C_2H_2 + C_2H \rightarrow C_4H_2 + H$	6,06E+17
$C_2H_2^+ + C_2H_2 \rightarrow C_4H_3^+ + H$	4,85E+17
$C_2H_2^+ + C_2H_2 \rightarrow C_2H_3^+ + C_2H$	4,25E+17
$C_2H_2^+ + C_2H_2 \rightarrow C_4H_2^+ + H_2$	2,61E+17
$C_2H_2 + C_2 \rightarrow C_4H + H$	2,15E+17
$C_2H_3^+ + C_2H_2 \rightarrow C_4H_3^+ + H_2$	1,52E+16
$H + C_2H \rightarrow C_2H_2$	5,43E+14
$C_2H_2^+ + C_2H \rightarrow C_4H_2^+ + H$	9,47E+13
$H_2 + H \rightarrow H + H_2$	6,1E+13
$C_4H_3^+ + C_2H \rightarrow C_6H_3^+ + H$	2,14E+13
$H + CH \rightarrow C + H_2$	1,47E+13
$C_4H_2^+ + C_2H \rightarrow C_6H_2^+ + H$	1,42E+13
$H + C_2H_3 \rightarrow C_2H_2 + H_2$	1,42E+13
$C_4H_2 + C_2H_2^+ \rightarrow C_4H_2^+ + C_2H_2$	1,23E+13
$C_4H_2 + C_2 \rightarrow C_6H + H$	1,23E+13
$C_4H_2 + C_2H \rightarrow C_6H_3$	1,1E+13
$C_2H_3 + C_2H \rightarrow 2 C_2H_2$	7,89E+12
$H_2 + C_2H^+ \rightarrow C_2H_2^+ + H$	4,21E+12

$C_2H_2^+ + C \rightarrow C_3H^+ + H$	2,1E+12
$C_2H_3 + C_2H_2^+ \rightarrow C_4H_3^+ + H_2$	2,1E+12
$C_2H + C \rightarrow C_3 + H$	1,58E+12
$H + C_4H_2^+ \rightarrow C_4H_3^+ + H$	9,82E+11
$C_4H_2^+ + C_4H_2 \rightarrow C_6H_2^+ + C_2H_2$	8,77E+11
$C_4H_2 + C_2H_2^+ \rightarrow C_4H_2^+ + C_2H_2$	8,77E+11
$C_4H_2 + C \rightarrow C_5H + H$	5,26E+11
$C_2H_3^+ + C_2H \rightarrow C_4H_3^+ + H$	4,21E+11
$C_2H^+ + C \rightarrow C_3^+ + H$	3,79E+11
$C_2H_3^+ + C_2H \rightarrow C_2H_2^+ + C_2H_2$	3,79E+11
$C_2H_3^+ + C_2H \rightarrow C_4H_2^+ + H_2$	1,75E+10
$H + C_2H_3^+ \rightarrow C_2H_2^+ + H_2$	0
$C_4H_3^+ + C \rightarrow C_5H_2^+ + H$	0
$C_4H_2^+ + C \rightarrow C_5H^+ + H$	0
$H + C_4H_3^+ \rightarrow C_4H_4^+ + H$	0
$C_4H_3^+ + C_4H_2 \rightarrow C_8H_5^+ + H$	0
$C_4H_2^+ + C \rightarrow C_5^+ + H_2$	0
$C_4H_3^+ + C_4H_2 \rightarrow C_6H_3^+ + C_2H_2$	0
$C_4H_3^+ + C \rightarrow C_5H^+ + H_2$	0
$H_2 + C_2H \rightarrow C_2H_2 + H$	0
$H + C_4H_2 \rightarrow C_4H_3$	0
$C_2H_3 + C_2H_2^+ \rightarrow C_2H_3^+ + C_2H_2$	0
$H_2 + C_2H_2^+ \rightarrow C_2H_3^+ + H$	0

$C_4H_2^+ + C_4H_2 \rightarrow C_8H_4^+ + H$	0
$C_4H_2^+ + C_4H_2 \rightarrow C_8H_3^+ + H$	0
$H_2 + H \rightarrow H + H_2$	0
$C_4H_2 + C_2H \rightarrow C_6H_2 + H$	0
$H_2 + H \rightarrow H + H_2$	0
$CH + C \rightarrow C_2 + H$	0

Table IV Surface reactions included in the model.

Surface Before	Surface After	Impinging Species	Released Species	Probability
<i>a-C</i>	<i>a-C:H</i>	<i>H</i>	–	0.9
<i>a-C:H</i>	<i>a-C</i>	<i>H</i>	<i>H₂</i>	0.1
<i>any</i>	<i>a-C</i>	<i>C₂</i>	–	1
<i>any</i>	<i>a-C</i>	<i>C</i>	–	1
<i>any</i>	<i>a-C:H</i>	<i>CH</i>	–	1
<i>a-C</i>	<i>a-C:H</i>	<i>C₂H</i>	–	1
<i>a-C</i>	<i>a-C:H</i>	<i>C₄H₂</i>	–	1
<i>a-C</i>	<i>a-C:H</i>	<i>C₄H₃</i>	–	1
<i>a-C</i>	<i>a-C:H</i>	<i>C₂H₃</i>	–	1
<i>a-C:H</i>	<i>a-C</i>	<i>C₂H</i>	<i>C₂H₂</i>	0.1
<i>a-C:H</i>	<i>a-C</i>	<i>ions</i>	<i>H</i>	0.1
<i>a-C:H</i>	<i>a-C:H</i>	<i>ions</i>	–	0.9
<i>any</i>	<i>any</i>	<i>Ar⁺</i>	<i>Ar, e</i>	1
<i>any</i>	<i>any</i>	<i>e</i>	–	1

8. List of figure captions

- Figure 1: (Top (a)) Mass spectrum generated from cracking pattern taken from the NIST database [53]. Each pattern was scaled relatively to the background level of its main peak in the spectrum below. (Bottom (b)) Mass spectrum in RGA mode with the plasma on (signal) and off (background) at 0.02 A, 0.66 Pa and 10 cm from the cathode with a ratio of 20 % C₂H₂ in logarithmic scale. Some possible species attributions are shown above prominent peaks.
- Figure 2: Main ion intensities from mass spectrometry (empty marker), compared with simulated ion densities in front of the substrate (filled marker) for different currents. Both point sets correspond to a fixed ratio of 20 % acetylene. The grey lines show linear fit applied to experimental and simulated values together (determination factors r^2 are shown in the legend). The spectrometer intensities in count s⁻¹ were converted to densities by multiplying by an arbitrary conversion factor (1.28×10^8 [m⁻³ s count⁻¹]) chosen to give the best overall fits.
- Figure 3: (Left) Intensity difference ($I_{plasma\ on} - I_{plasma\ off}$) of main RGA mass spectrometric peaks at 0.02 A, 0.66 Pa, and 10 cm from the cathode with varying acetylene ratio. (Right) Simulation S₁ main radicals' densities after 16 μs for different acetylene ratios. The arrows represent the expected relative evolution of concentrations as the reactive H and C₂H get consumed in reactions producing C₄H₂ and H₂.
- Figure 4: Main ions intensities from mass spectrometry plotted against the acetylene ratio for a fixed current set at 0.016A with a distance of 18 cm between the mass spectrometer and the magnetron.

- Figure 5: Intensity of main ions peaks measured with the mass spectrometer vs the total chamber pressure in a discharge with 4 % acetylene and a current set at 100 mA.
- Figure 6: Vertically clipped view of the electron density after 40 μs in a simulation with 20 % acetylene in the 3D meshed chamber used in the simulation. Distances are in mm and density is color coded in m^{-3} . Each colored point corresponds to a simulation cell. Cells with electron density below $1 \times 10^{13} \text{m}^{-3}$ were hidden. The bounding box axis is graduated in millimeters.
- Figure 7: Mean densities of several species' vs the distance from the cathode surface in millimeters in simulation S_1 (20 % acetylene, and 0.8 W). Each curve corresponds to one time-step of 1 μs from 0 (blue) to 40 μs (yellow)
- Figure 8: Carbon and acetylene ion density in the chamber cut with a vertical plane and absorption profiles on the chamber walls in the S_1 simulation after 40 μs .
- Figure 9: Mean densities of principal species and species groups as a function of the distance from the cathode [mm] in simulation S_1 (20 % acetylene, and 0.8 W) after 40 μs of simulation.
- Figure 10: Mean densities of all charged (Top) and neutral species (Bottom) in the plasma bulk of several simulations after 20 μs , with varying acetylene ratio (Left) and power (Right). The different line types are underlying the similar evolutions of several groups of species: the first order (plain), second order (dot-dashed), and other species (dashed).

9. Figures

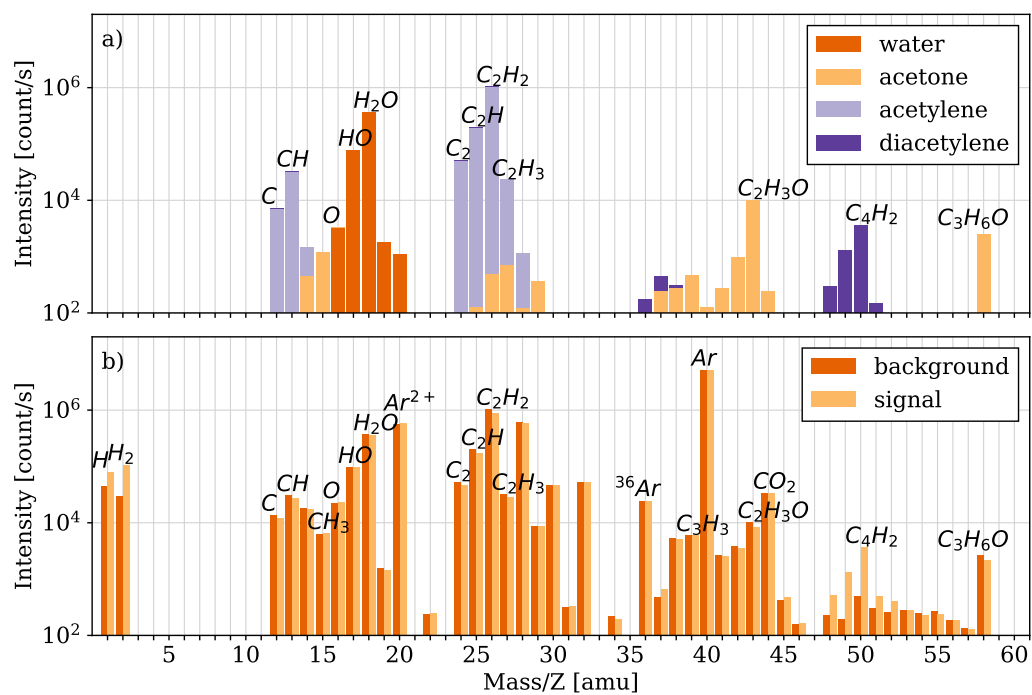


Figure 1

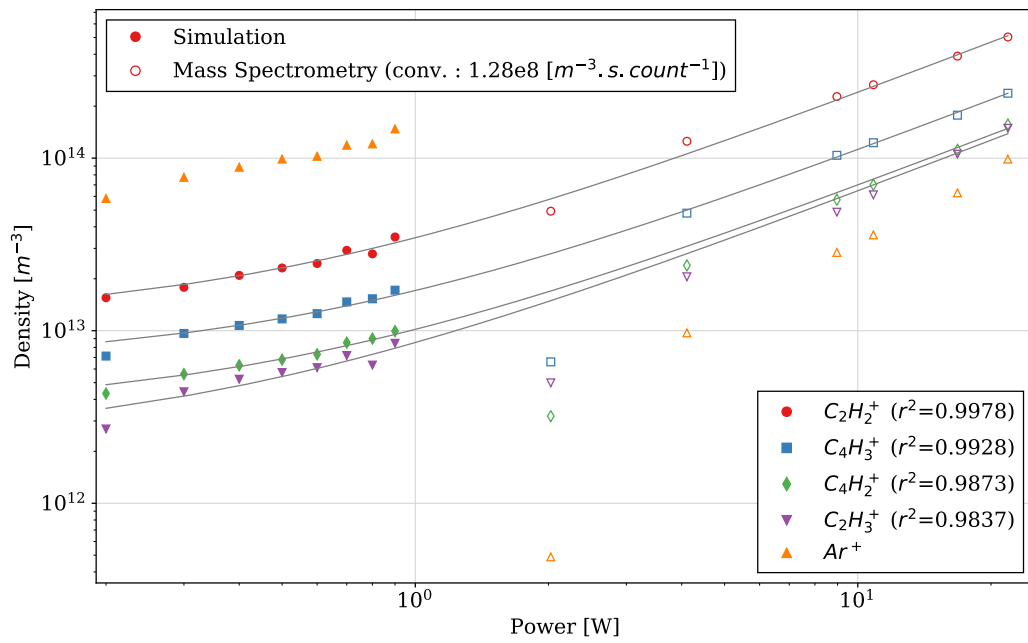


Figure 2

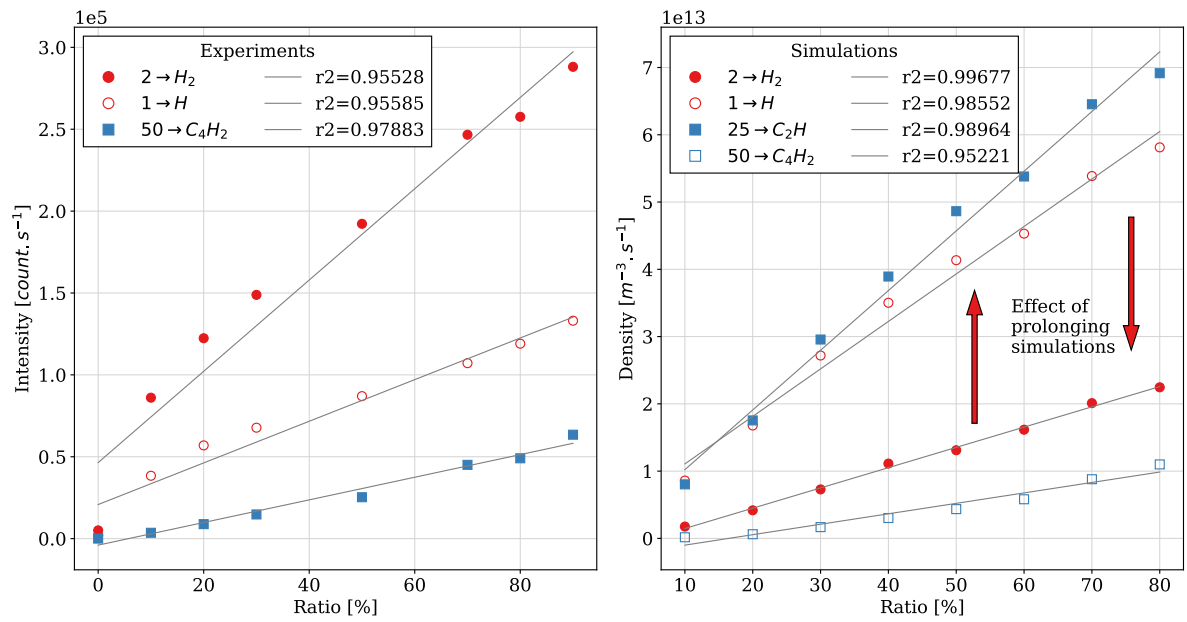


Figure 3

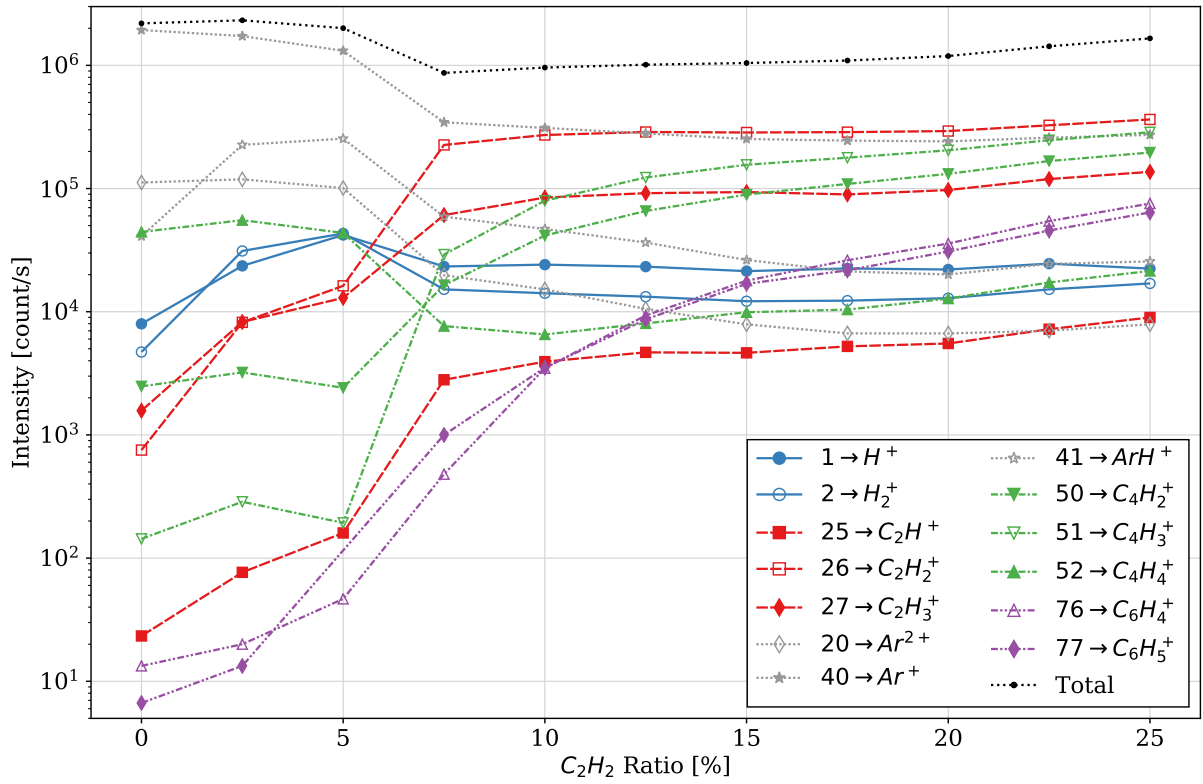


Figure 4

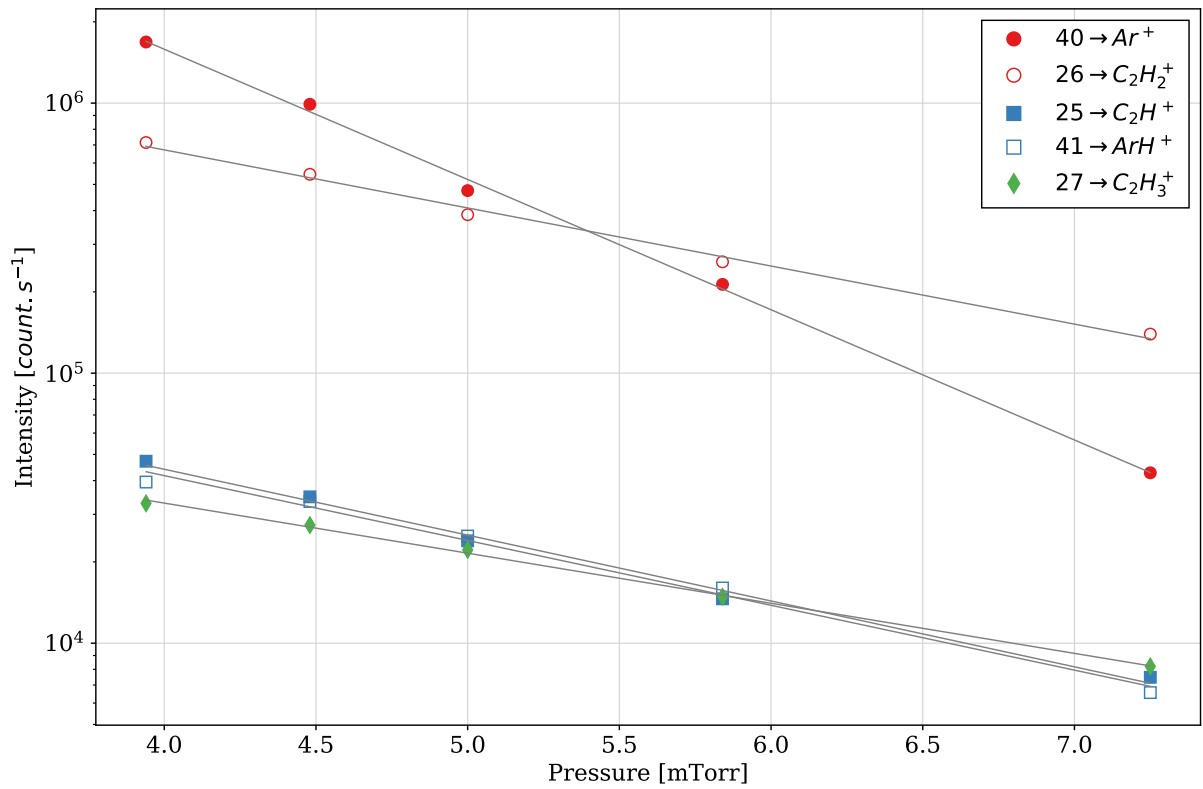


Figure 5

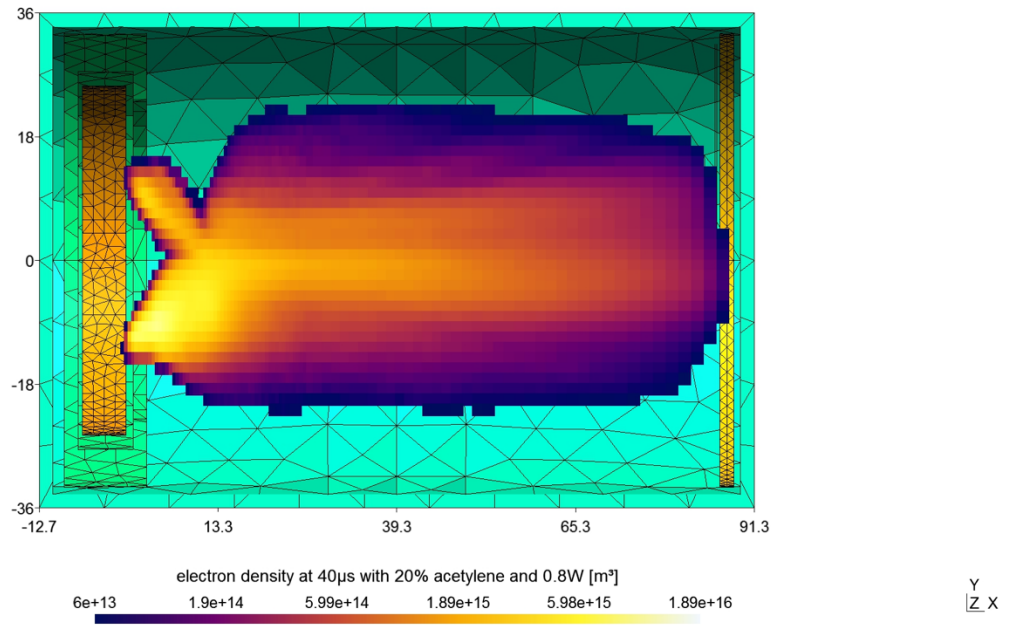


Figure 6

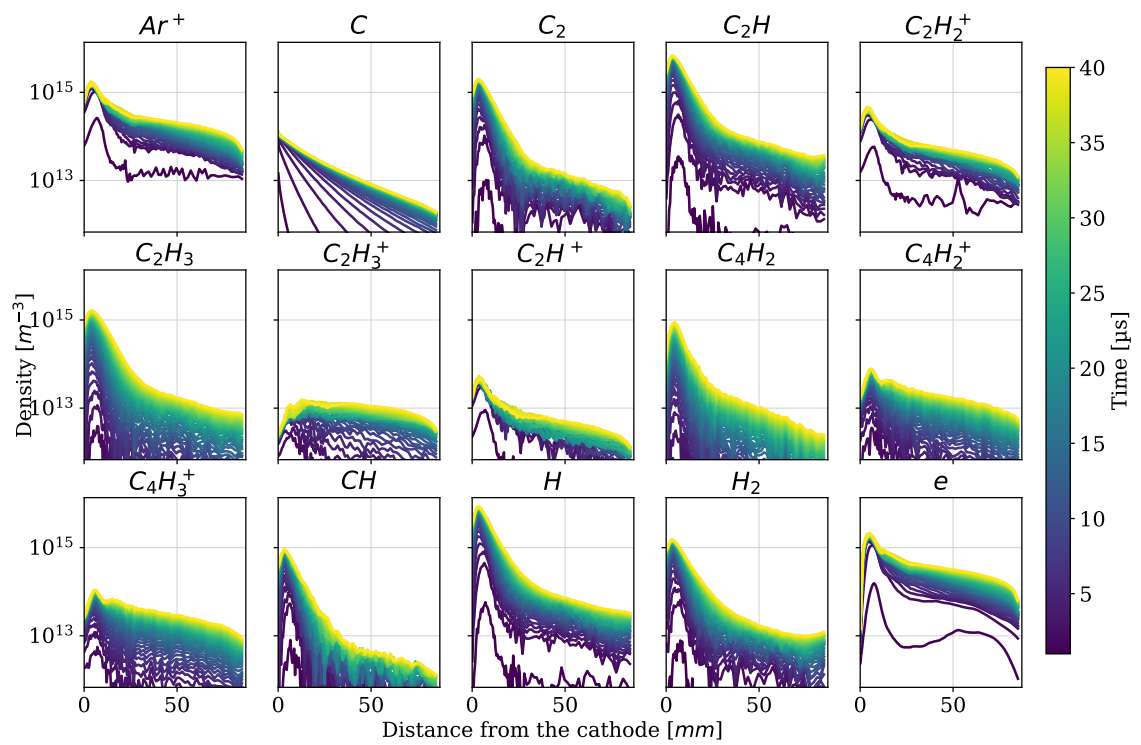


Figure 7

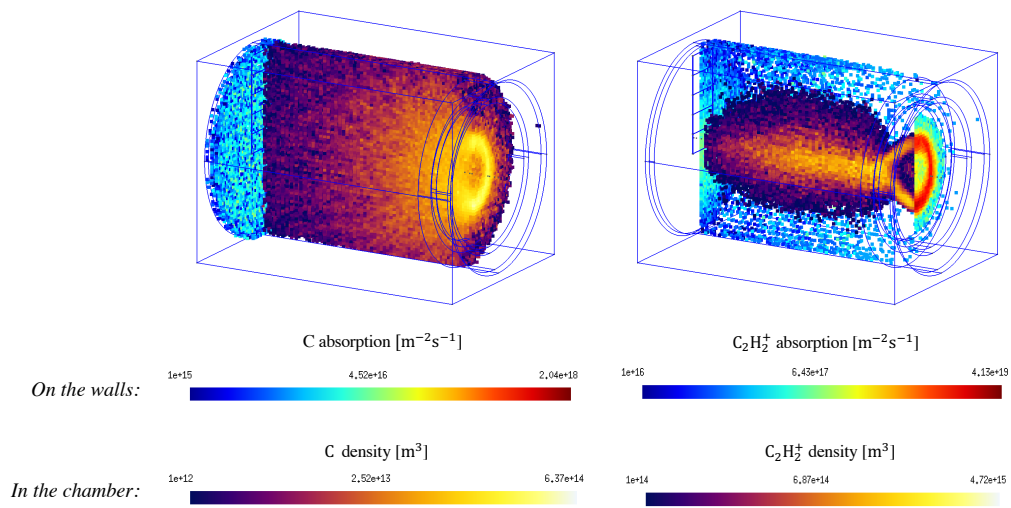


Figure 8

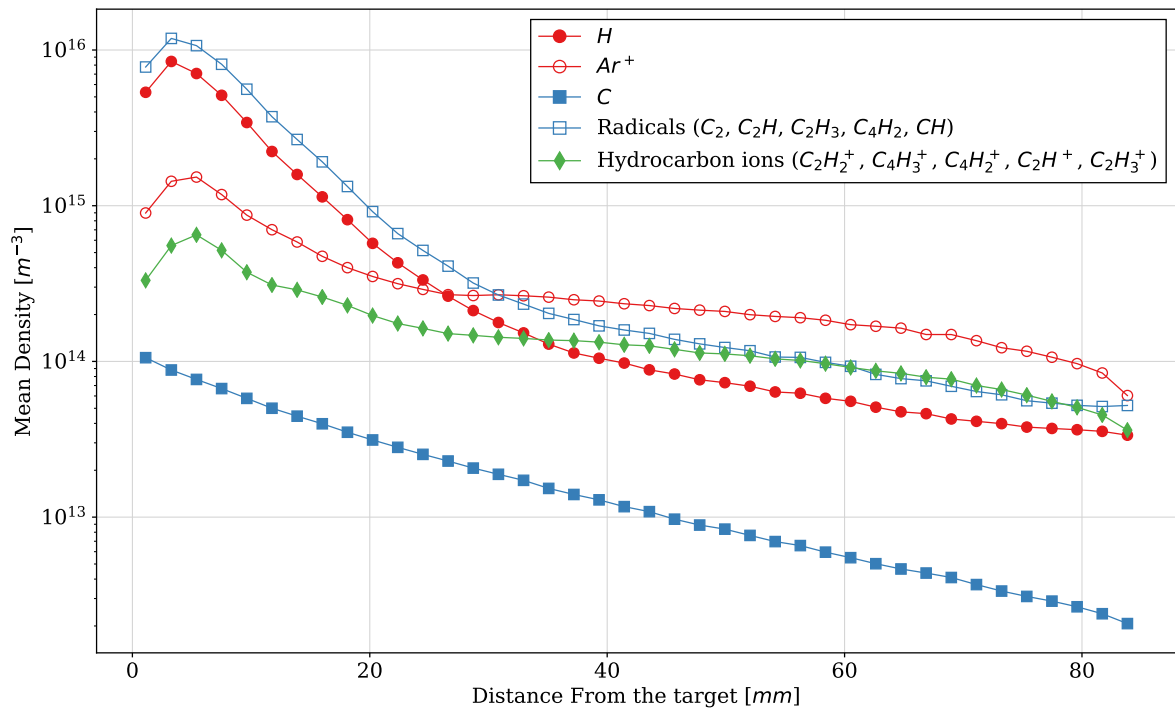


Figure 9

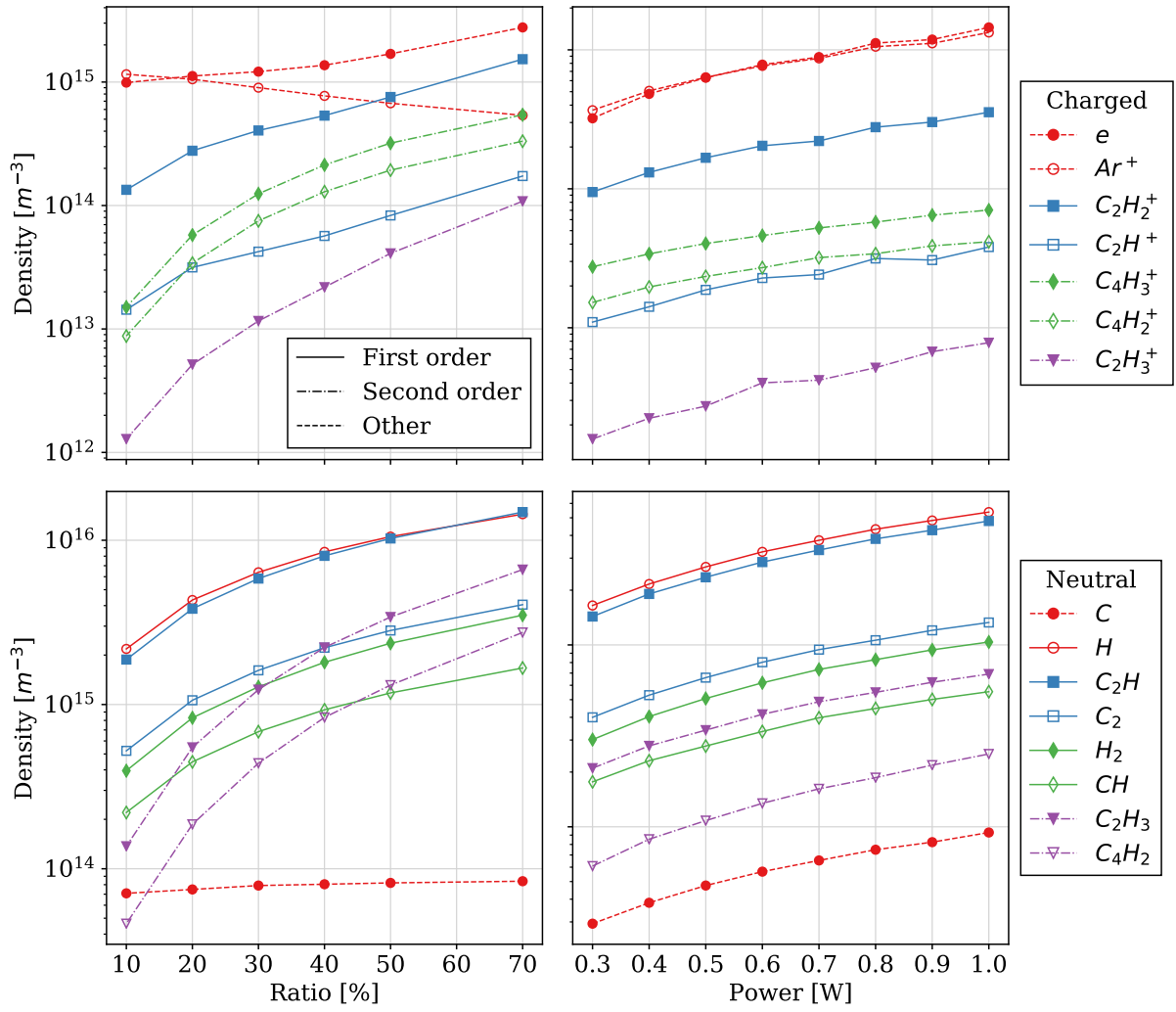


Figure 10